M 2023

U.PORTO
FEUP FACULDADE DE ENGENHARIA
UNIVERSIDADE DO PORTO

CFD PROCESS DESIGN FOR PHOTO-ASSISTED PRODUCTION OF GREEN AMMONIA-BASED FUELS

MARIA TERESA PIMENTA DE FREITAS MATOS DE OLIVEIRA
MASTER THESIS IN CHEMICAL ENGINEERING
PRESENTED TO THE FACULTY OF ENGINEERING
OF THE UNIVERSITY OF PORTO

Master in Chemical Engineering

CFD process design for photo-assisted production of green ammonia-based fuels

Master dissertation

of

Maria Teresa Pimenta de Freitas Matos de Oliveira

Developed within the course of dissertation

held in

LSRE-LCM - Laboratory of Separation and Reaction Engineering – Laboratory of Catalysis and Materials

Supervisor at FEUP: **Doctor Ricardo Jorge Nogueira dos Santos**

Joint supervisors at FEUP: **Professor Cláudia Sofia Castro Gomes da Silva**

Doctor Margarida Sarmento e Cunha Abrunhosa de Brito

U.PORTO
FEUP FACULDADE DE ENGENHARIA
UNIVERSIDADE DO PORTO

DEPARTAMENTO DE
ENGENHARIA QUÍMICA

July 2023

Agradecimentos

Em primeiro lugar, mostro o meu extremo agradecimento aos meus orientadores, o Senhor Doutor Ricardo Santos e Senhoras Doutoras Cláudia Silva e Margarida Brito, pelo apoio contínuo e aconselhamento próximo que me ofereceram durante estes meses. Observar alguém com tanto conhecimento, experiência e gosto pela ciência é tão motivador quanto gratificante.

Estendo os meus sinceros agradecimentos ao laboratório LSRE-LCM, nomeadamente ao Senhor Professor Joaquim Faria, na qualidade de Coordenador Científico, que me permitiu desenvolver a dissertação dentro de um ambiente extraordinário e de uma equipa com um talento excecional.

Um agradecimento especial à Bondalti, na pessoa da Senhora Doutora Filipa Franco, pela disponibilidade e acompanhamento prestado.

Agradeço também à Isabel Barbosa e à Isabel Fernandes pelo apoio, pela prontidão em ajudar e pela simpatia constante.

Um agradecimento aos companheiros do gabinete 3.11, por todas as dicas, conversas e gargalhadas, que fizeram com que o semestre passasse ainda mais rápido.

Às minhas amigas de sempre: obrigada por fazerem tudo valer a pena. Que sorte termos cruzado os nossos caminhos. Mal posso esperar para ver onde a vida nos leva!

Em último lugar, ainda que sempre em primeiro plano, deixo uma nota especial aos meus pais: ver o vosso orgulho é a maior gratificação que o meu trabalho alguma vez me poderia oferecer. Tudo o que faço e tudo o que sou é por vós.

This work was financially supported by LA/P/0045/2020 (ALiCE), UIDB/50020/2020 and UIDP/50020/2020 (LSRE-LCM), and by the project SuN2Fuel 2022.04682.PTDC - funded by national funds through FCT/MCTES (PIDDAC).

Fundação para a Ciência e a Tecnologia

SuN2Fuel Photo-assisted production of green ammonia-based fuels

REPÚBLICA PORTUGUESA

Abstract

With a global shift towards an energy system transformation and an escalating demand for renewable energy sources, there is an increased need for long-term storage solutions that can counter-balance intermittent energy production. Ammonia rises as a promising low-carbon fuel and efficient hydrogen carrier, easy to store and to be used for clean direct electricity generation. This work aims to study the performance of a mesostructured photocatalytic reactor and its viability as a small-scale industrial reactor for green-ammonia production.

The 3D prismatic geometry of a unitary element of the structured reactor, i.e., the DeanCell, is designed through Computational Fluid Dynamics (CFD) tools, namely the ANSYS R2 2022 software. The study of velocity and vorticity profiles along the length of the cell enables to optimise its configuration, by evaluating the mixing degree and the preferential paths of the flow of the fluid phase. This hydrodynamic study revealed that the chosen configuration of the DeanCell promotes the formation of dynamic structures, i.e. Dean vortices, mainly on the step expansion drawn on the structure.

Mass transfer simulations were performed to establish the maximum limits for mass transfer within the unit-cell, to guarantee that the operation of the structured device is under chemical regime. An immobilisation study was carried out to assess the influence of the catalyst position on the ammonia diffusion throughout the reactor. Sherwood numbers evaluated the mass transport and showed that product diffusion is only slightly dependent on the localization of the catalytic material. The reaction between N_2 and H_2 was also modelled, in gas phase. No validated kinetic parameters were used in these simulations, and so the data retrieved is only an approximate estimative of the results. Nevertheless, the reaction heat and the temperatures reached inside the DeanCell are too high to enable the use of graphitic carbon nitride as the catalyst, which requires the additional modelling of heat transfer through the walls.

Final process modelling simulations using Aspen Plus V12.1 used CFD output data to simulate the integration of the photocatalytic reactor in a complete ammonia synthesis loop, using N_2 and H_2 as the feed stream components. The analysis of the operational costs of the process indicates a competitive energy consumption value, with respect to other renewable ammonia plants. Further studies are required, however, for the validation of the CFD model through experimental data, to more accurately simulate the photocatalytic reaction.

Keywords: green-ammonia; photocatalysis; structured reactor; CFD; process simulation.

Resumo

Face à crescente preocupação por uma transição do sistema energético, urge, cada vez mais, a procura de soluções de armazenamento energético de longo prazo, de forma a contrabalançar a produção intermitente de energia associada aos recursos renováveis. O amoníaco surge, neste cenário, como uma alternativa promissora, dado que se constitui como um combustível de baixo teor em carbono e um transportador eficiente de hidrogénio, fácil de armazenar e de ser utilizado em células de combustível. O presente trabalho tem como objetivo estudar o desempenho de um reator fotocatalítico meso-estruturado e avaliar a sua viabilidade como um reator industrial (de pequena escala) para a produção de amoníaco verde.

A geometria prismática 3D de um elemento unitário do reator estruturado (a DeanCell) é projetada e otimizada com recurso a ferramentas de Dinâmica dos Fluidos Computacional (CFD). O estudo dos perfis de velocidade e vorticidade ao longo da célula permitem otimizar a configuração da geometria, através da avaliação do grau de mistura e do escoamento da fase fluida. O estudo da hidrodinâmica da célula permite concluir que a geometria da DeanCell, e principalmente, o degrau desenhado na estrutura, provocam a criação de um escoamento secundário, na forma de vórtices de Dean, que intensifica a mistura dentro do reator.

O objetivo principal das simulações de transferência de massa realizadas foi avaliar quais os limites máximos para a transferência de massa dentro da DeanCell, a fim de garantir a operação do sistema em regime químico. Um estudo de imobilização foi realizado para avaliar a influência da posição do catalisador na difusão do amoníaco ao longo do reator. O cálculo de números de Sherwood foi utilizado para avaliar o transporte de massa, e permitiu concluir que a difusão do produto é apenas ligeiramente dependente da localização do material catalítico. A reação entre o N_2 e H_2 foi simulada em fase gasosa. Nenhum parâmetro cinético foi validado, pelo que os dados obtidos são apenas uma estimativa aproximada dos resultados. No entanto, o calor da reação e as temperaturas atingidas dentro da DeanCell são demasiado altas para permitir o uso de nitreto de carbono grafítico como catalisador, o que requer a simulação adicional da transferência de calor através das paredes.

Os resultados obtidos pelas simulações em CFD foram utilizados no software Aspen Plus V12.1, de forma a integrar o reator fotocatalítico num sistema de síntese de amoníaco, através de N_2 e H_2. A análise dos gastos operacionais do processo indica um valor favorável e competitivo para o consumo de energia em relação a outros processos de produção de amoníaco verde. No entanto, estudos futuros requerem a validação do modelo de CFD desenvolvido através de dados experimentais, de modo a simular mais corretamente a reação fotocatalítica.

Palavras-chave: amoníaco verde; fotocatálise; reator estruturado; CFD; simulação do processo.

Declaration

I hereby declare, under word of honour, that this work is original and that all non-original contributions are indicated and due reference is given to the author and source.

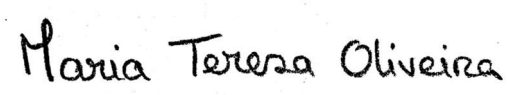

2 de julho de 2023

Index

List of Figures

List of Tables

Notation and Glossary

A	pre-exponential factor	$mol \cdot m^{-2} \cdot s^{-1}$
c	order of accuracy of the Richardson's extrapolation method	
C_f	*inlet concentration of tracer*	*kmol·m-3*
C_s	outlet concentration of tracer	$kmol \cdot m^{-3}$
C_{CP}	ammonia concentration in the catalytic plate	$kmol \cdot m^{-3}$
Co	Courant number	
C_{out}	ammonia concentration at the outlet face	$kmol \cdot m^{-3}$
d	height of the inlet and outlet channels of the cell	m
D	height of the main channel of the cell	m
D_m	mass diffusivity coefficient	$m^2 \cdot s^{-1}$
D_h	hydraulic diameter	m
$E(\theta)$	residence time distribution curve	
E_a	activation energy	$kJ \cdot mol^{-1}$
$F(\theta)$	Danckwerts' curve	
F	total force	$N \cdot m^{-3}$
F_b	body forces	$N \cdot m^{-3}$
F_s	external surface forces	$N \cdot m^{-3}$
g	gravitational force	$m \cdot s^{-2}$
j	number of compression stages	
k	mass transfer coefficient	$m \cdot s^{-1}$
L	length of the main channel of the cell	m
l_{CP}	length of the catalytic plate	m
l_{in}	length of the inlet and outlet channels of the cell	m
M	molecular weight	$g \cdot mol^{-1}$
N	molar flux	$kmol \cdot m^{-2} \cdot s^{-1}$
n	*number of layers*	
p	pressure	Pa
ΔP	pressure drop	Pa
P_1	initial pressure before compression stage	Pa
P_2	final pressure after compression stage	Pa
r	growth rate	
Re	Reynolds number	
Sc	Schmidt number	
Sh	Sherwood number	
t	time	s
t_r	mean residence time	s
Δt	time-step size	s
ΔT_{min}	minimum temperature approach	K
T	temperature	K
v	velocity	$m \cdot s^{-1}$
v_{in}	injection velocity	$m \cdot s^{-1}$
$v_{max,out}$	maximum velocity at the outlet face	$m \cdot s^{-1}$
V	molar volume of the solute at its normal boiling point	m^3
V_d	dead volumes inside the cell	m^3
w	width of the inlet and outlet channels of the cell	m
W	width of the main channel of the cell	m
Δx	mesh element size	m
$\Delta x_{first\ layer}$	thickness of the first inflated layer of the mesh	m
X_{N2}	conversion of N_2 to NH_3	
Y_i	mass fraction of the species *i*	

Greek Letters

β	aspect ratio	
ε	emissivity	
ζ	dimensionless z coordinate	
η	dimensionless y coordinate	
θ	dimensionless time	
ξ	dimensionless x coordinate	
λ_B	Batchelor scale	
λ_K	hydrodynamic scale	
μ	kinematic viscosity	Pa·s
μ_d	dynamic viscosity	$m^2 \cdot s^{-1}$
ρ	density	$kg \cdot m^{-3}$
τ	residence time	s
τ_w	wall shear stress	Pa
Φ	solvent factor	
Φ_{ext}	extrapolated solution through Richardson's extrapolation method	
$\Phi_{\Delta x}$	numerical solution of a mesh with element size Δx	
$\Phi_{2\Delta x}$	numerical solution of a mesh with element size $2\Delta x$	
$\Phi_{4\Delta x}$	numerical solution of a mesh with element size $4\Delta x$	

Indexes

i	number of species
$-$	average

List of Acronyms

CAD	Computer-aided Design
CB	Conduction Band
CFD	Computational Fluid Dynamics
CFL	Courant-Friedrichs-Lewy
FCT	Fundação para Ciência e Tecnologia
LCM	Laboratory of Catalysis and Materials
LSRE	Laboratory of Separation and Reaction Engineering
MUSCL	Monotonic Upstream-centred Scheme for Conservation Laws
N-S	Navier-Stokes
NRR	Nitrogen Reduction Reaction
OER	Oxygen Evolution Reaction
OPEX	Operational Expenses
PFR	Plug Flow Reactor
RKS-BM	Redlich-Kwong-Soave-Boston-Mathias
RTE	Radiative Transfer Equation
RTD	Residence Time Distribution
SMR	Steam Methane Reforming
UFD	User-Defined Function
UV	Ultraviolet
VB	Valence Band

1 Introduction

1.1 Framing and presentation of the work

Ammonia (NH_3) is the second most produced chemical worldwide, with an annual production of approximately 150 million tons and main application in the manufacturing of fertilisers (Yüzbaşıoğlu et al. 2022).

The conventional industrial route for ammonia synthesis predominately follows the Haber-Bosch process, which works under severe conditions of temperature (400-500ºC) and pressure (up to 250 bar) and is accountable for the consumption of almost 2% of global annual energy and the emission of 1.2% of total CO_2 annual emissions (Society 2020, Han et al. 2022).

The ammonia synthesis industry is predicted to keep growing, supported by continued population growth (estimated to increase by 25% until 2050) and projections of significant economic development over the next decades (UN 2022). This persistent and sustained demand for ammonia increases the likelihood of the emergence of potential new markets.

As countries transition to a new energy basis, reliant on intermittent renewable sources (like sunlight and wind), it is crucial to use long-term energy storage to offset this discontinued production. The use of ammonia as a chemical energy carrier and an on-demand energy producer, with possible direct use in fuel cells or as a low-carbon fuel, can significantly reshape the current energy landscape and power generation space.

While most of NH_3 production is carried out through steam reforming of natural gas, this massive increase in ammonia demand motivated the search for modern and more sustainable alternatives, also driven by current environmental pressures and ambitious political actions towards an effective action against climate change (Smith et al. 2020).

Heterogeneous photocatalysis for nitrogen (N_2) fixation represents a promising route towards the green production of ammonia through renewable resources, such as air and water, and solar light or lower energy-consumption radiation sources (such as LEDs) for catalyst photoactivation (Chen et al. 2018).

This project aims to simulate and optimise the best unitary cell configuration of a meso-structured catalyst immobilised photoreactor through Computational Fluid Dynamics (CFD) simulations and data processing. Given the complexity of the photocatalytic process, due to the interaction of different physical models, such as mass transfer, reaction kinetics, and photon flux distribution, CFD tools arise as a helpful design strategy to predict and optimise fluid behaviour inside the photoreactor (Elyasi and Taghipour 2010).

Thus, this work aims to evaluate the mass transfer limiting rates that guarantee the system's operation under chemical regime. An estimation of operation costs was performed to assess the viability of the process at an industrial scale, particularly facing such a well-integrated and heavily industrialised process as the Haber-Bosch.

1.2 Contribution of the author to the work

This dissertation was carried out in the framework of the project SuN2Fuel - 2022.04682.PTDC, funded by FCT- Fundação para a Ciência e Tecnologia, I.P., under the guidance and supervision of Doctors Ricardo Santos, Cláudia Silva and Margarida Brito. The author of this work performed all the numerical simulations. The base geometry of the unitary cell, used and further optimised in CFD simulations, was previously generated by Isabel Barbosa and Doctor Margarida Brito.

1.3 Organization of the dissertation

The layout of this dissertation is presented as follows.

Chapter 2 gives a brief context to the work. Conventional routes for ammonia synthesis and current research on photocatalytic materials and technologies are presented. Previous reports on CFD simulation of photocatalytic devices and research on structured reactors for mixture enhancement are also explored in this section.

Chapter 3 includes all simulation input data and models used. After a short presentation of the equations behind CFD modelling in section 3.1, the geometry of the unitary element used as a base case for all simulations is shown, along with the mass transfer and Residence Time Distribution (RTD) models used in FLUENT simulations.

The main results of the simulations are given in Chapter 4. Reynolds tests are performed to characterise the hydrodynamic behaviour of the fluid inside the cell. The residence time distribution is also evaluated, through tracer injection experiments (Section 4.2). Mass transfer limitations are assessed through species modelling, both in liquid and gas phases (Section 4.3) and a catalyst immobilisation study is performed in order to study the influence of the catalyst position inside the cell on the mass transfer phenomena. Ammonia synthesis reaction is modelled on section 4.4.

A techno-economic integration of the photocatalytic process is performed using ASPEN software and CFD data, and the main simulation outputs are shown in Chapter 5.

2 Context and State of the art

2.1 Ammonia Synthesis: conventional and alternative routes

Fritz Haber's work on nitrogen fixation from the air, further developed and modified by Carl Bosch, is considered one of the most significant technological advances of the 20th century and was the first industrial process to propose the use of high-pressure to force a chemical reaction (Chen et al. 2019).

The overall process consists of circulating nitrogen and hydrogen over an iron-based catalyst at high pressure and temperature to promote the reaction. Natural gas or coal are typically used as feedstocks for hydrogen (H_2) production, which is obtained via a process of steam methane reforming (SMR), inherently responsible for a large share of the overall carbon oxide (CO and CO_2) emissions and energy consumption of the process (Smith, Hill et al. 2020).

The reversible reaction for ammonia synthesis

$$N_2 + 3\,H_2 \rightleftharpoons 2\,NH_3 \tag{1}$$

is exothermic and thereby favoured by low temperatures (Modak 2002).

However, low temperature negatively affects the reaction rate, as it delays nitrogen bond dissociation over the catalyst. Therefore, a compromise temperature of 400-450°C and pressure of 200 atm, together with the use of a catalyst, ensure that the reaction proceeds with sufficient yield (15%) (Smith, Hill et al. 2020).

This low single-pass conversion of the reaction is unattractive from a productivity point of view. The process uses an ammonia synthesis recycle loop, where unreacted gases are compressed and returned to the reactor, as shown in Figure 1, to achieve a higher conversion of 97% after several passes. In the final step, a condenser liquefies and separates NH_3 (Modak 2002).

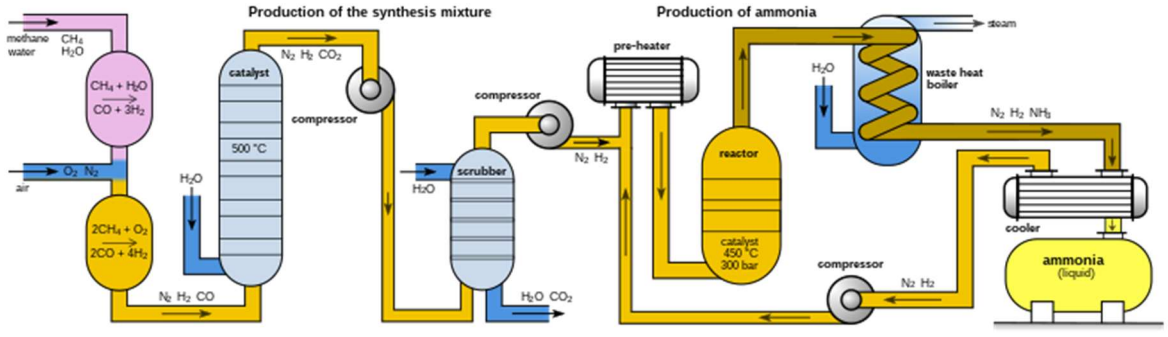

Figure 1- Overview of the Haber-Bosch process. (Pirie 2019)

Haber-Bosch's feed routes, the compression stage, and the refrigeration cycle intensify the energy requirement of the process and motivate the search for more sustainable alternatives.

Electrolysis-based ammonia processes are not new and accounted, in 1930, for around one-third of overall global production. Renewable ammonia can be produced via water electrolysis (for hydrogen production) coupled with Haber-Bosch's synthesis loop (IRENA and AEA 2022).

Direct ammonia synthesis from hydrogen and nitrogen through electrochemical processes has also been under study. Solid and molten electrolytes get special attention due to their resistance under high temperatures that favours the ammonia synthesis reaction. Marnellos and Stoukides (1998) first reported, in 1998, the use of a solid proton-conducting cell-reactor for NH_3 production at 570°C and atmospheric pressure. Over 78% of the hydrogen flown over the anode was electrochemically transferred (as H^+) to a palladium cathode, where it reacted with N_2 to produce ammonia, as schematised in Figure 2.

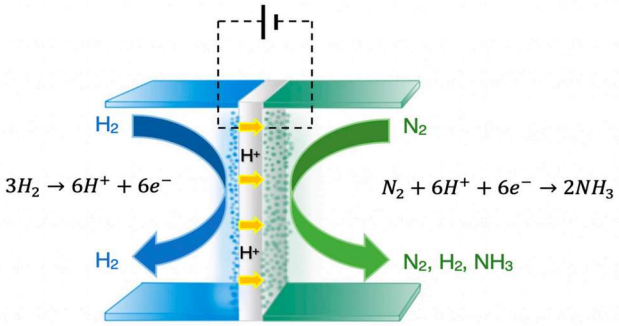

Figure 2- Schematic diagram of an electrochemical cell for NH_3 production from H_2 and N_2. (Garagounis et al. 2019)

However, the recombination reaction of atomic hydrogen into H_2 is faster than the reaction with atomic nitrogen, which affects the overall efficiency of the system (Garagounis, Vourros et al. 2019).

In spite of still requiring fundamental research and being far from industrial-level production rates, ammonia synthesis through photocatalysis is a promising alternative to the energy-intensive Haber-Bosch process, being based on sustainability pillars and in the use of clean technologies and renewable resources.

2.2 Photocatalysis for ammonia production

Heterogeneous photocatalysis is an emerging technology for nitrogen fixation. Recent research focuses on using cost-effective materials and efficient radiation sources, such as sunlight, to produce ammonia from water and nitrogen gas at ambient operating conditions.

According to the band gap theory of semiconductors, these have a banded structure characterised by a dense valence band (VB) of electrons of the outermost shell and a conduction

band (CB) of higher energy. The potential difference between these two bands (the bandgap energy) is slight in photocatalysts. Under irradiation, and only if the energy absorbed is greater or equal than the bandgap energy, electrons (e^-) travel to the CB, leaving a hole (h^+) in the VB. This creates energy carriers (i.e., electrons and holes) that migrate to the active sites in the material surface and interact with other adsorbed species (Shen, Yang et al. 2022).

This electron transfer between the semiconductor and the adsorbed reagents is thermodynamically limited by the redox potential of these species. Electron-accepting species adsorbed on the surface can only be reduced by the electrons in the CB if their redox potential is more positive than the redox potential of the band. Likewise, a donor species can only be oxidised by the holes in the VB if its potential is more negative) (Amaral 2016).

NH_3 photocatalytic synthesis comprises two different but interlinked conversion steps: oxygen evolution reaction (OER) and N_2 reduction reaction (NRR), respectively.

$$3\,H_2O\,(l) + 6\,h^+ \rightarrow \frac{3}{2}\,O_2(g) + 6\,H^+(aq) \quad (2)$$

$$N_2\,(g) + 6\,H^+\,(aq) + 6e^- \rightarrow 2\,NH_3(g) \quad (3)$$

However, photon-driven fixation of N_2 is affected by the weak adsorption and activation of the molecules on the catalyst surface (Chen, Li et al. 2018). Even though it is an abundant and stable substance, the direct use of the N_2 molecule is often a problem due to the high energy of the triple bond (944 kJ·mol^{-1}). The major energy constraint is thus associated with the first electron transfer from the photocatalyst to the N_2 molecule, which has the most negative redox potential (-4.16V) and is needed to destabilise the triple bond. The NRR step is thought to be carried out by forming higher energy intermediates, such as N_2H_2 and N_2H_4, via proton-coupled electron transfer (Shen et al. 2022).

2.2.1 Current research on catalytic materials

Semiconductor materials are used in photocatalysis, and the efficiency of these processes strongly relies on the structure design and on the catalysts used (Ansari et al. 2019).

TiO_2 is one of the most common semiconductors that has been used extensively since the work of Formenti et al. (1971). It is non-toxic, of easy access and of high chemical stability. It shows higher reaction rates than other metal oxides (such as zinc (II) and tin (IV)) when applied to organic compounds degradation (Dharma et al. 2022). However, a critical point in this catalyst's efficiency is its wide band gap energy (3.0-3.2 eV), which translates into inaction or poor material activity when exposed to visible light. In fact, less than 5% of the solar light spectrum can be used for this catalyst's activation (Vaiano et al. 2020).

Besides, the recombination of photo-excited electron-hole pairs can also compromise the efficiency of the reaction. Much as 90% of these pairs recombine, and so the number of photo-induced carriers available at the surface is limited (Hernández-Alonso et al. 2009).

To overcome this problem, sacrificial agents (usually electron donors, like amines and alcohols) are added to the system to suppress this phenomenon (Shen et al. 2020). Structural modifications such as doping the material or combinations with other semiconductors can also be performed to reduce the bandgap and the recombination of energy carriers.

Metal-doping of TiO_2 has been reported in several studies as a way to optimise its electronic properties and upgrade the material's sensitivity to visible light.

Schrauzer and Guth (1977) first addressed the impact of different metal dopants on TiO_2 photocatalytic activity, specifically applied to the case of N_2 photo-fixation, under UV irradiation, at 40°C. Samples doped with iron oxide (Fe_2O_3) revealed greater reaction yields, followed by Co, Mo and Ni oxides.

The work of Sato and White (1980) experimentally reported the catalytic decomposition of water on a powdered platinised TiO_2 (Pt/TiO_2) catalyst. Noble metal doping alters the surface of the semiconductor, acting as a trap for photo-excited electrons and inhibiting electron-hole recombination, as schematised in Figure 3, for the specific case of CO_2 photoreduction to methane.

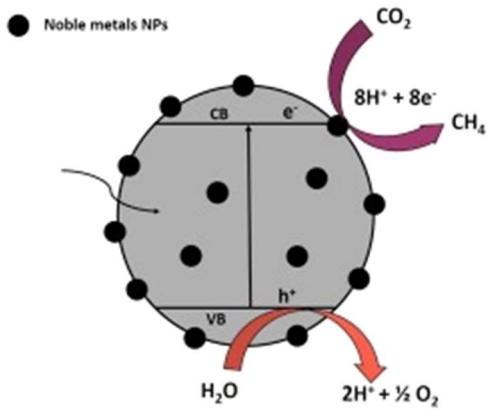

Figure 3- Metal-modified semiconductor photocatalyst particle. Reprinted with permission from (Singhal and Kumar 2017). Copyright 2017. Elsevier.

The affinity of transition metals and N_2 electronic structures is shown to facilitate the binding of these two species, making it appealing for the photoreduction of the molecule (Shen, Yang et al. 2022). A significant increase in doped iron ions concentration can have the opposite and undesirable effect on creating more recombination sites, inhibiting the reaction (Li et al. 2020).

Recent research has revealed other highly efficient alternatives to common photocatalysts for nitrogen reduction.

Graphitic carbon nitride (g-C_3N_4) is a non-metal semiconductor that has shown good photocatalytic activity when applied to the removal of NO_3^- in wastewater treatment (Zhang et al. 2020). It offers good electronic properties, chemical stability and a narrow bandgap energy of 2.7 eV. However, surface modification of this polymer is often needed to increase surface area and inhibit recombination phenomena. This explains why most studies involve metal-doped nanosheets of the polymer (Nguyen et al. 2021).

It is important to note that NH_3 synthesis through NO_3^- reduction is an easier route than through N_2, due to the higher solubility of the nitrate and to the fact that the cleavage energy of the N—O bond is 21.68% smaller than that of N—N (Hao et al. 2021).

Nonetheless, Hao, Ren et al. (2021) have reported enhanced light adsorption and electronic conductivity, as well as faster electron-hole separation rates, when using g-C_3N_4 nanosheets doped with metallic ruthenium. These samples showed an effective 92.85% NO_3^- elimination through several irradiation cycles and higher photocatalytic activity than bulk g-C_3N_4.

Higher photocatalytic ammonia synthesis was also shown when coupling g-C_3N_4 nanosheets with magnesium oxide (10 wt.%) and FeOCl.

2.2.2 Challenges and current solutions for photoreactors

Due to the complex nature of mixing phenomena and the limitations of mass transfer and light distribution in photocatalytic processes, the industrialization of this type of technologies is still under study (Adesina 2004). The typical laboratory-scale photoreactors are the annular and the flat plate reactor, which are appropriate for kinetic and performance studies, but cannot withstand typical industrial flow inputs (Boyjoo et al. 2017).

On what concerns the catalyst state, slurry-type photoreactors are usually preferable to immobilised photocatalysts, in terms of efficiency, due to higher surface-to-volume ratio and less mass transfer limitations. These require, however, an additional catalyst separation step that increases the cost of a full-scale industrial plant (Starosud et al. 1999).

Micro and mesostructured reactors are widely applied in the chemical engineering area, due to their potential to enhance mixing and reaction rates and easy scalability. These small-scale reactors are especially interesting in the synthesis of organic compounds and polymeric materials, broadening their applicability to biological and pharmaceutical fields (Bojang and Wu 2020).

Mesostructured reactors are characterised by small dimensions at the order of millimetres. Because of this, these devices operate at laminar chaotic flow regimes, which is advantageous

as it enhances the mass and heat transfer mechanisms, minimises the amount of reagents needed, operates in a safer mode and enables the more precise control of reaction variables (Barbosa et al. 2023).

Aside from efficient catalysts and adequate light sources, photocatalytic reactions are much conditioned by the fluid dynamics and the dimensions and geometry of the photoreactor. The small characteristic length, typical of the composing elements of the reactor, enables more uniform light and flow distribution, thus mitigating the impact of possible stagnant or non-irradiated zones on the reaction efficiency. Besides, higher heat and mass transfer rates are achieved with this type of reactor (Kayahan et al. 2020).

Light attenuation effect when scaling-up the photoreactor must also be kept in consideration. As stated by the Beer-Lambert Law, the absorbance of radiation by the reaction medium depends on the distance from the light source, also known as the optical path length. Therefore, for photoreactors with larger dimensions, the radiation distribution is less uniform (Donnelly and Baumann 2021). Structured reactors are an effective approach to process intensification since the scale-up from laboratory level to pilot and industrial scale is carried out by numbering up the unit elements of a network of meso and microchannels, and not by increasing the overall cell dimension, which keeps constant the surface/volume ratio and does not affect the high characteristic mass and heat transfer performance of these reactors.

This type of reactors has been previously applied to photocatalytic processes.

Lima et al. (2016) used the *NETmix*® technology, which consists of a structured network of chambers and channels, for the photocatalytic treatment of water contaminated with antibiotics. The reactor's configuration allows for better control of mixing and mean residence time of the reagents, consequently increasing the efficiency of the pollutant degradation reaction (da Costa Filho et al. 2017).

Silva et al. (2022) also reported the application of a brass-mesh structured reactor, immobilised with TiO_2, on textile dye photodegradation. The high surface area of the monoliths enables a higher load of catalyst deposited on the surface, enhancing the photocatalytic efficiency and showing good performance and stability after consecutive cycles.

2.3 CFD Modelling of Photocatalytic Reactors

Despite the apparent effectiveness of laboratory-scale reactors, commercial systems for photocatalytic ammonia synthesis are still much under development, especially when confronted with the Haber-Bosch process, one of the greatest achievements in the chemical industry.

CFD tools are able to model the system's hydrodynamics and the interaction of the flow phase with the catalyst, making it easier to develop or optimise already existing real-scale reactors while minimising experimental and economic effort (Duran et al. 2011).

However, photoreactor modelling is hindered by the several physics models associated with photocatalysis. Besides predicting hydrodynamics (flow and mixing patterns), special attention should be given to the irradiance distribution (through the Radiative Transfer Equation, RTE) and to the photochemical kinetics of the reaction and the catalyst at study. CFD simulations are an effective way to approach a numerical solution that accounts for the complex interaction of all these phenomena (Elyasi and Taghipour 2010).

There are few reports on CFD studies for photocatalytic ammonia synthesis simulation. Nevertheless, there has been some research on the application of CFD in modelling photocatalytic reactors for the treatment of air and water streams.

Duran, Mohseni et al. (2011) reported a study on CFD modelling of immobilised annular reactors for photocatalytic benzoic acid degradation in water. It was shown that the first-order reaction rate was limited by mass transfer in the system. On the catalyst's boundary zones, surface rates were nearly zero, due to insufficient UV irradiation.

Deng et al. (2023) used CFD tools to analyse photocatalytic oxidation in gas-phase reactors, which showed that internal baffles could strongly increase residence time, impacting the velocity field and improving the reaction in the bulk. The lamps and the reactors were placed concentrically, allowing for good symmetry of the radiation intensity along all the length.

An experimental flat plate reactor with immobilised TiO_2 catalyst for phenol removal in wastewater streams was designed by Ahmed et al. (2022). A 3D model of the prototype was used to analyse phenol concentration at the outlet, following a specific degradation rate of 0.17 min^{-1}. The numerical results were compared to experimental data and proved to accurately simulate the flow and measure outlet concentration of the organic compound, with only a difference of 5% between both results. It was also reported that the inlet position is a critical point in the creation of recirculation zones, which strongly affect the mixing at the fluid-catalyst interface and therefore impact the efficiency of the reaction.

Sengupta et al. (2001) simulated fluid flow instability in an immobilised photocatalytic reactor through the creation of Taylor-Couette vortices between two rotating coaxial cylinders. This phenomenon was shown to enhance photocatalytic oxidation efficiency, as degradation rates were higher with respect to other reactors designed for the same pollutant. The two compounds showed very different kinetic constants but were degraded at the same rate, proving diffusion was the controlling step of the reaction.

Similarly, a study on the influence of secondary flows in reactors with curved channels or with disturbance obstacles was published by Lira et al. (2022). Different geometries were evaluated, and it was observed that the velocity profile was changed when in comparison to the typical parabolic curve of straight channels. The presence of Dean's vortices induces an increase in the centrifugal force in the tubes, shifting the maximum velocity near the outer wall, where the catalyst is immobilised, thus increasing mass transfer coefficients.

3 CFD Models and Validation

3.1 Governing Equations

Computation Fluid Dynamics (CFD) is now a critical part of the design of chemical processes and reactors, as it enables a fuller understanding of the phenomena inside the systems. Modelling of chemical reactors follows several key components that enable to simulate fluid behaviour and to retrieve data on chemical reaction and heat and mass transfer. These computational tools use a numerical approach to solve a set of partial differential equations (otherwise difficult to solve analytically) that mathematically model the flow of a viscous and incompressible (Newtonian) fluid: the Navier-Stokes (N-S) Equations.

These equations are based on mass, momentum and energy conservation principles. The solution to the N-S equations for a fluid flow is a velocity and pressure field. Over the flow field, other physical phenomena can be simulated, such as chemical reaction or heat conduction.

The Eulerian form of the continuity equation states that, for a fixed control volume, the mass of the flow remains constant over time. The continuity equation is given by

$$\frac{\partial \rho}{\partial t} + \rho\,(\nabla \cdot \boldsymbol{v}) = 0 \tag{4}$$

where $\boldsymbol{v}$ is the velocity vector and ρ is the density of the fluid.

The equation for momentum conservation is a result of Newton's second law. The force, $\boldsymbol{F}$, exerted on the fluid particle per unit of volume, is given by

$$\boldsymbol{F} = \rho \cdot \frac{\partial \boldsymbol{v}}{\partial t} \tag{5}$$

There are two main forces that can act on a fluid: the body forces ($\boldsymbol{F_b}$), such as gravity, dependent only on its mass, and the external surface forces ($\boldsymbol{F_s}$), due to pressure, p, and the effects of the fluid's viscosity, μ. The Navier-Stokes equation then takes its most general form, following

$$\rho\left(\frac{\partial \boldsymbol{v}}{\partial t} + \boldsymbol{v} \cdot \nabla \boldsymbol{v}\right) = \rho \boldsymbol{g} - \nabla p + \mu \nabla^2 \boldsymbol{v} \tag{6}$$

To study diffusion inside the reactor and to evaluate the limits of mass transfer, the species transport model equation is given by

$$\frac{\partial Y_i}{\partial t} + \nabla \cdot (\boldsymbol{v} Y_i) = D_m \nabla^2 Y_i \tag{7}$$

where Y_i is the local mass fraction of species i, and D_m is the mass diffusion coefficient for species i in the fluid mixture. The right-hand side of the equation represents the diffusive term, modelled by default through Fick's Law and variable with concentration and temperature. The solution of convective and diffusive terms gives the relative mass fraction of each chemical species in the fluid domain.

3.2 Geometry

The structured reactor addressed in this work consists in a network of unit cells with the same geometry of the one shown in Figure 4. The reactor's unit cell, i.e., the DeanCell, was designed to promote the formation of Dean vortices, that intensify the mixing inside the reactor. This geometry was drawn in Design Modeler, one of the CAD (computer-aid design) modules available in ANSYS R2 2022.

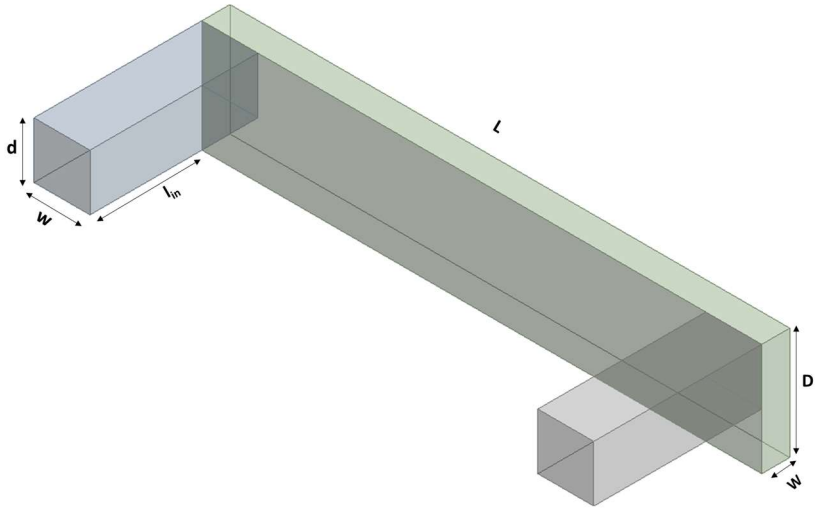

Figure 4- Geometry of the DeanCell used in CFD simulations.

The geometry shows three different bodies: inlet channel, outlet channel, and the main body, where the catalyst is immobilised at the walls. Both channels have a cross-section area of 1x1 mm^2 (*d* and *w*). In a preliminary study, both channels had a length of 6mm. However, CFD simulations showed that a length, l_{in}, of 3 mm is enough to obtain a fully developed laminar velocity profile at the inlet channel. This change did not show a significant impact on the outputs of the simulation nor on the velocity profiles along the channels (as explored in section 2 of Appendix A), but it significantly decreased the computation time required for the simulations.

Other dimensions were set from preliminary CFD simulations, performed at a Reynolds number (Re) of 100, and vorticity maps were traced in order to optimise the dimensions of the main body. Vorticity profiles along the length of the cell show that the step drawn on the structure causes an increase in this variable, enhancing mixing in this cell region. The case promoting

better vorticity was shown to be a cell with 10mm of length, *L*, *D* of 2mm and *W* of 0.5mm, which was kept for all simulations as the optime base geometry.

3.3 Domain Discretization

Domain discretization is a critical point of the CFD pre-processing stage, as it affects the accuracy of the CFD simulation. Different mesh grids and types of mesh elements show different numerical diffusion levels, distorting the solution accuracy (Sosnowski 2018).

For the present work, a structured grid with pure hexahedral elements was generated. The meshing process was performed with Meshing, a module available in ANSYS R2 2022 that discretises the CAD geometry in a numerical mesh. The MultiZone method was used to guarantee the decomposition of the geometry in all its three single body parts.

Additional inflation was added to the four lateral walls of the main body and at the two connecting faces. Finer grid layers are needed to better describe the gradients at the walls where the catalyst is immobilised and thus increase the solution accuracy. First layer thickness model was used for inflation control, with a fixed value of 12 layers and a growth rate equal to 1.2.

Figure 5 shows different views of the generated mesh, with particular detail on the inflation in the walls of the main body.

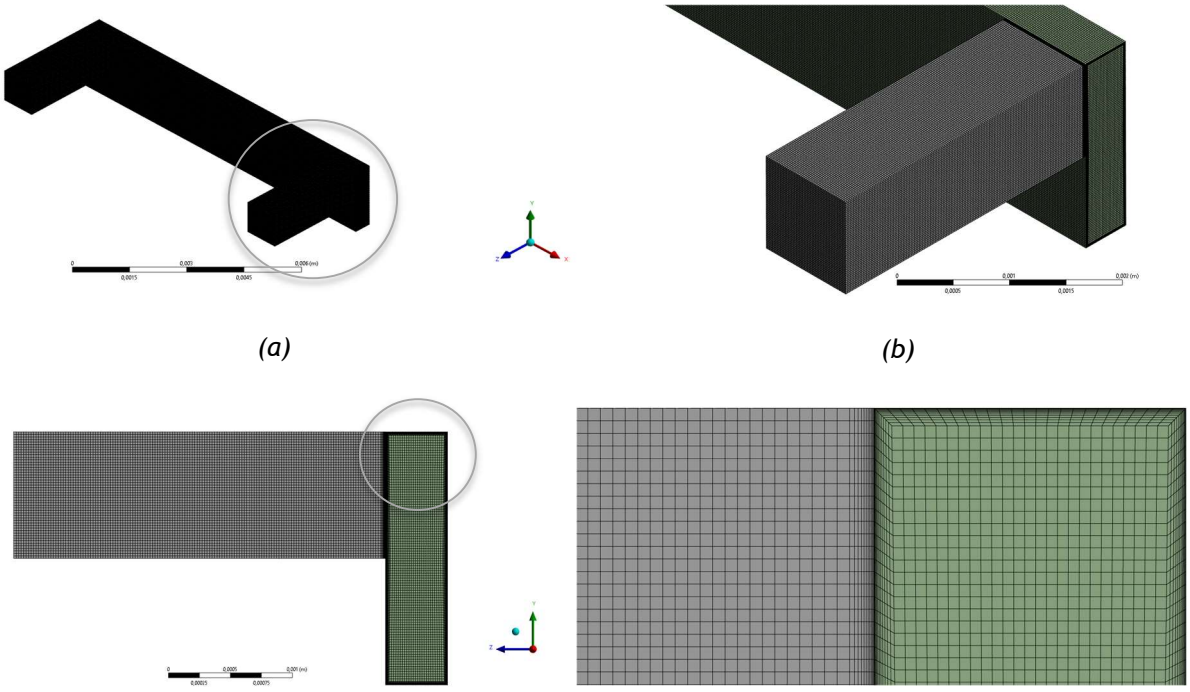

(a) *(b)*

(c) *(d)*

Figure 5- Overall (a) and side-view (c) of the generated mesh for the DeanCell; Detailed view of the inflation layers (b,d).

To further define boundary conditions on CFD simulations, named selections were created for the different walls of the DeanCell. The walls of the main body where the catalyst is immobilised are identified in the following Figure 6, as the bottom, top, interior and exterior walls.

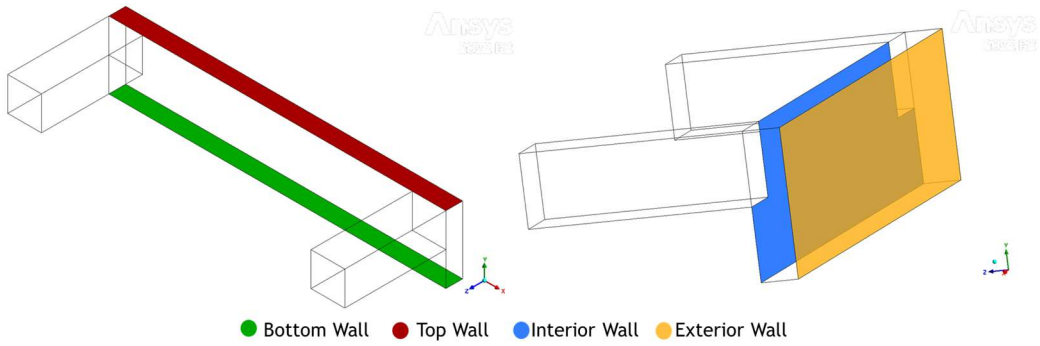

Figure 6- Named selections created in Meshing.

3.3.1 Mesh Validation

To ensure the independency of the solution from the mesh, both the mesh element size, Δx, and first layer thickness for the inflation were varied and further evaluated.

The computation time increases with the total number of elements in the model. Yet, in more refined meshes, the computed results are much closer to the proper solution. A compromise between the simulation time and solution accuracy must be found in order to choose an appropriate mesh size.

For the grid independence test, the working fluid is set as water, at 20°C, and the following default physical properties were set: a density of 998.2 kg·m^{-3} and a kinematic viscosity of 1x10^{-6} m^2·s^{-1}.

The test was performed at $\mathrm{Re} = 250$ to assess the influence of element size in the CFD solution. A condition of constant atmospheric pressure is imposed at the outlet, and the no-slip condition is applied to the walls. As the injection velocities are low, laminar flow was considered for all simulations.

A fully developed velocity profile was previously settled in ANSYS/Fluent through a user-defined function (UDF) at the inlet. As the inlet channel is a square duct, the hydraulic diameter, D_h, a parameter needed to compute injection velocity, is considered equal to the edge of the inlet face. The UDF guarantees that a fully developed laminar flow profile is established at the inlet, and is given by

$$\frac{v^*(x,y)}{v_{in}} = \frac{\sum_{n\ odd}^{\infty}\sum_{m\ odd}^{\infty}\frac{\sin(n\pi\xi)\sin(m\pi\eta/\beta)}{nm\,(\beta^2n^2+m^2)}}{\sum_{n\ odd}^{\infty}\sum_{m\ odd}^{\infty}\frac{4}{\pi^2n^2m^2(\beta^2n^2+m^2)}} \tag{8}$$

where v_{in} is the inlet velocity. A deeper insight into this function is given in Appendix A.1.

The criteria for the grid independence test are the maximum velocity at the outlet face, $v_{max,out}$, the pressure drop between the inlet and outlet of the DeanCell, ΔP, and the shear stress at the walls, τ_w. Table 1 lists the variation of these three parameters with the grid size.

Table 1- Influence of mesh element size on simulation parameters.

Mesh	Δx /m	First inflation layer thickness /m	Number of elements	$v_{max,out}$ / m·s^{-1}	ΔP /Pa	τ_w / Pa
A	2 x 10^{-5}	1 x 10^{-5}	3.56 x 10^{6}	0.509	-324.29	2.66 x 10^{-4}
B	2 x 10^{-5}	1 x 10^{-6}	3.55 x 10^{6}	0.500	-324.93	2.66 x 10^{-4}
C	4 x 10^{-5}	1 x 10^{-6}	6.44 x 10^{5}	0.502	-325.12	2.64 x 10^{-4}
D	5 x 10^{-5}	1 x 10^{-6}	3.76 x 10^{5}	0.503	-323.76	2.59 x 10^{-4}
E	8 x 10^{-5}	1 x 10^{-6}	1.39 x 10^{5}	0.493	-322.13	2.51 x 10^{-4}
F	1 x 10^{-4}	1 x 10^{-6}	7.84 x 10^{4}	0.489	-317.26	2.41 x 10^{-4}

Richardson's extrapolation method is used to compute an accurate solution based on the numerical solutions of the different grids. This method can be applied to calculate an estimation of the exact value, when a variation of a certain parameter (in this case, the mesh element size, Δx) gives result to different numerical solutions. To keep a constant refinement ratio of 2 between the element size, meshes B, C and E were selected as the coarse, the medium and the fine mesh for the test. The numerical solutions for these grids, $\Phi_{\Delta x}$, $\Phi_{2\Delta x}$ and $\Phi_{4\Delta x}$ are used to extrapolate the numerical solution, Φ_{ext}, through

$$\Phi_{ext} = \frac{2^c \Phi_{\Delta x} - \Phi_{2\Delta x}}{2^c - 1} \tag{9}$$

With *c* being the order of accuracy of the model, calculated by

$$c = \frac{\ln \frac{\Phi_{4\Delta x} - \Phi_{2\Delta x}}{\Phi_{2\Delta x} - \Phi_{\Delta x}}}{\ln 2} \tag{10}$$

Figure 7 shows the mesh independence graphics using this numerical analysis. The extrapolated value is highlighted in red in all graphs.

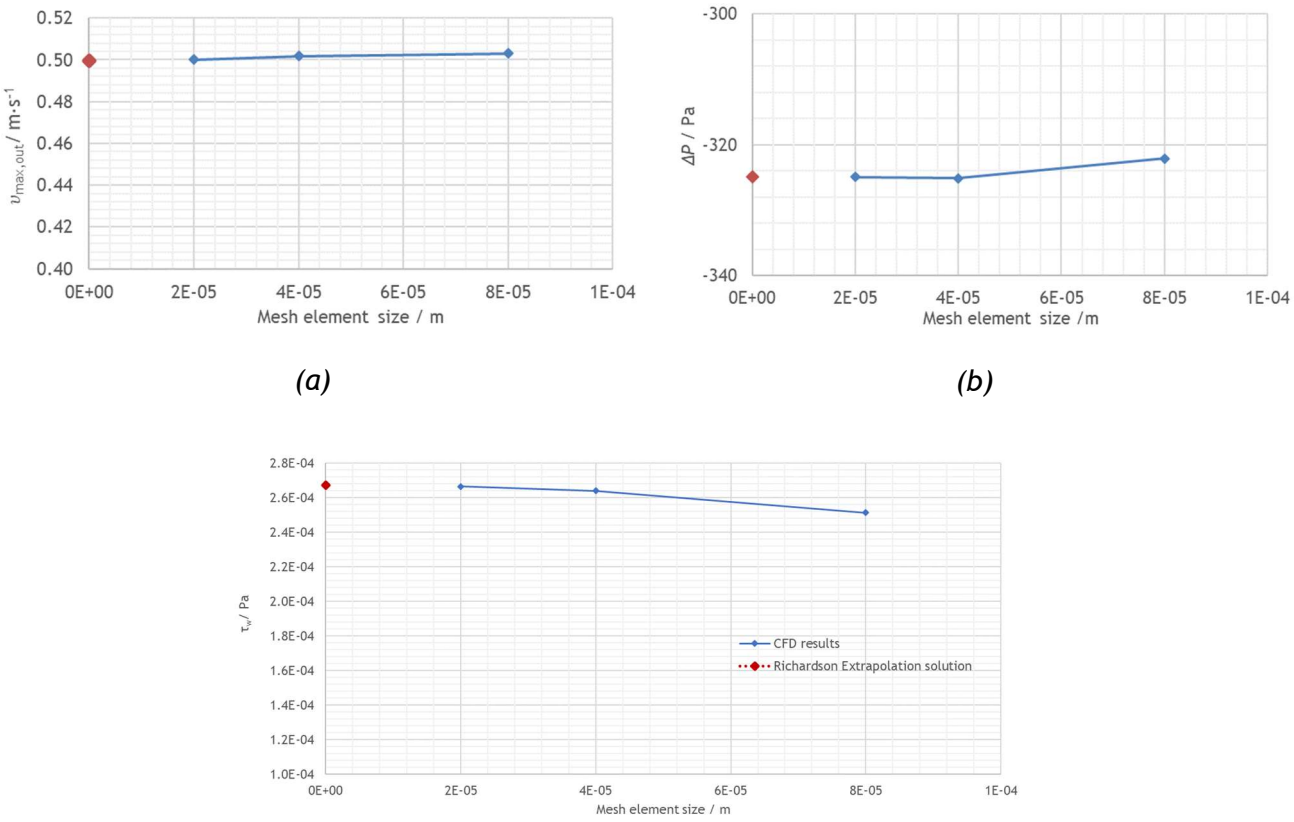

(a) *(b)*

(c)

Figure 7- Richardson Extrapolation method for mesh element size study.

The variation in the results due to the element size of the mesh can be observed not to be significant, with mesh B showing the best results, with deviations of only 0.12%, 0.01% and 0.32% from the extrapolated solution for $v_{max,out}$, ΔP and τ_w, respectively.

This leads to conclude that, despite not being the most refined mesh, mesh B ($\Delta x = 2\text{x}10^{-5}$ m) gives numerical solutions that are accurate and closer to the true value, making it appropriate for use in the simulations.

3.4 Mass Transfer CFD Model

3.4.1 NH_3 diffusion through the reactor

To simulate the diffusion and the mass transfer in the fluid phase, CFD simulations are carried out at different Reynolds numbers, using ANSYS Fluent R2 2022.

Considering the phenomena of ammonia diffusion from the catalytic surface to the bulk of the DeanCell, the species transport model is activated to create a mixture of NH_3 and H_2O. The density of the mixture, ρ, is calculated through the volume-weighted-mixing-law method, according to

$$\rho = \frac{1}{\sum_i \frac{Y_i}{\rho_i}} \tag{11}$$

In turn, the mass-weighted-mixing law method is used to compute the viscosity of the mixture, μ, by a simple mass fraction average of the viscosities of the pure species that form the mixture, through

$$\mu = \sum_i Y_i \mu_i \tag{12}$$

The mass diffusivity coefficient, D_m, is estimated in 2.32 × 10^{-9} $m^2 \cdot s^{-1}$, using Wilke and Chang's (1955) correlation for diffusive coefficients in dilute solutions,

$$D_m = 7.4 \times 10^{-8} \frac{\sqrt{\Phi \mathrm{M}}\, \mathrm{T}}{\eta\, \mathrm{V}^{0.6}} \tag{13}$$

where Φ is the association factor for the solvent (2.26, in the case of water), *M* is the molecular weight of the solvent, *T* is the temperature in K, η is the solution viscosity in cP, and *V* is the molar volume of the solute at its normal boiling point, i.e., NH_3 in this work.

The main goal of this work is to assess the limitations of the mass transfer inside the DeanCell, by estimating the maximum quantity of ammonia that can be released at the outlet of the unit-cell under the simulated conditions. To that end, mass transfer is simulated and the influence of the position of the immobilised catalyst at the reactor's walls is evaluated. Analysing the scenario of an infinite reaction, i.e., considering only mass transfer phenomena and assuming that the reaction does not limit the system, the maximum value of 2.4×10^{-5} for the mass fraction of NH_3 in water was defined as the boundary condition at the walls where the catalyst is immobilised. This value considers an immediate N_2 conversion to NH_3, and thus was calculated considering the stoichiometry of the production reaction and the solubility of nitrogen in water, at 20 ºC and 1 atm, which is 20 $mg \cdot dm^{-3}$ (Perera 2017).

CFD simulations were performed for injection velocities of 0.25 $m \cdot s^{-1}$ $(\mathrm{Re} = 250)$ and 0.35 $m \cdot s^{-1}$ $(\mathrm{Re} = 350)$. These values were calculated following the equation

$$Re = \frac{\rho\, v_{in}\, D_h}{\mu} \tag{14}$$

To assess the mass transfer from the wall to the fluid phase, mass transfer coefficients, k, were calculated for each working condition. Considering a well-mixed solution, the molar concentration gradient between the catalyst and the bulk of the reactor, ΔC, is the difference between the concentration in the catalytic plate (C_{CP}) and the monitored concentration value at the outlet face (C_{out}). Thus, the molar flux ($\dot{N}$) is given by

$$\dot{N} = k \cdot \Delta C = k \cdot (C_{CP} - C_{out}) \quad (15)$$

From the molar flux and the length of the catalytic plate, l_{CP}, the value of the Sherwood number, Sh, for each simulation, can be calculated through

$$Sh = \frac{k\, l_{CP}}{D_m} \quad (16)$$

This dimensionless number relates the convective and diffusive mass transfer from the walls to the bulk.

3.5 Residence Time Distribution Model

Residence time distribution (RTD) enables to evaluate the nonideality of a system, namely the presence of stagnant zones, bypasses, etc., and its real mixing characteristics. The real total time spent by fluid molecules inside the reactor is measured through tracer experiments, where a tracer with similar properties is injected and tracked over time.

Transient CFD simulations were performed for RTD experiments. The water flow inside the reactor at $\mathrm{Re} = 250$ (v_{in}= 0.25 m·s^{-1}) was previously simulated for the grid independence study. The species transport model was activated to perform the tracer simulations, and a mixture of H_2O and tracer, with a mass diffusivity of 2.32 × 10^{-9} m^2·s^{-1} (as previously calculated) was considered as the working fluid. The tracer was injected at the inlet and the initial conditions correspond to the reactor full of water and hydrodynamics previously calculated at steady state.

The time-step size (Δt) defined for the transient simulations was calculated from the Courant-Friedrichs-Lewy (CFL) condition, using the velocity, v, and the mesh element size, Δx, according to

$$\mathrm{Co} = \frac{v \Delta t}{\Delta x} \quad (17)$$

where Co is the Courant number. This value is dependent on the Reynolds number, Re, since it depends on the velocity. A Courant number (Co) of 1 was used in all simulations, i.e., in a given time step, the flow moves across an entire cell.

According to Equation 17, and for a Re of 250, the time step defined for this condition is equal to 8 × 10^{-5} s. Regarding the simulation time, it was the time needed to stabilise in a stationary state, which is equal to five times the residence time, τ.

The cumulative distribution function is monitored using CFD results from the following expression

$$F(\theta) = \frac{C_s(\theta)}{C_f} \tag{18}$$

where θ is the dimensionless time, $\theta = \frac{t}{\tau}$, $C_s(\theta)$ is the concentration of tracer at the outlet face and C_f is the inlet concentration of tracer. From the $F(\theta)$ curve, the RTD is determined, according to

$$E(\theta) = \frac{d[F(\theta)]}{d\theta} = \frac{d[C_s(\theta)]}{d\theta} \tag{19}$$

This curve considers the different times that different fluid elements take to travel through the cell, given as function of θ. The mean residence time for the molecules inside the cell, $\bar{t_r}$, can be estimated by

$$\bar{t_r} = \int_0^\infty t\, E(t)\, dt \tag{20}$$

4 CFD Results of the Photocatalytic Reactor

4.1 Hydrodynamics

As mentioned, CFD simulations were performed with two different Re, $\mathrm{Re} = 250$ and $\mathrm{Re} = 350$. For these conditions, the flow is laminar and so the N-S equations were fully resolved, i.e. there was no sub grid-scale model for turbulence.

The velocity function (Equation 8) defined from the UDF was used to guarantee a parabolic velocity profile at the entrance of the inlet channel. No other boundary conditions were set at the walls, except for the no-slip condition.

Prior to mass transfer studying, flow characterisation is essential to understand the behaviour of the fluid phase inside the cell. Velocity maps show the flow field and allows to evaluate the vorticity in the reactor. Figures 8a) and 8b) illustrate the velocity contours traced for the flow, for $\mathrm{Re} = 250$ and $\mathrm{Re} = 350$.

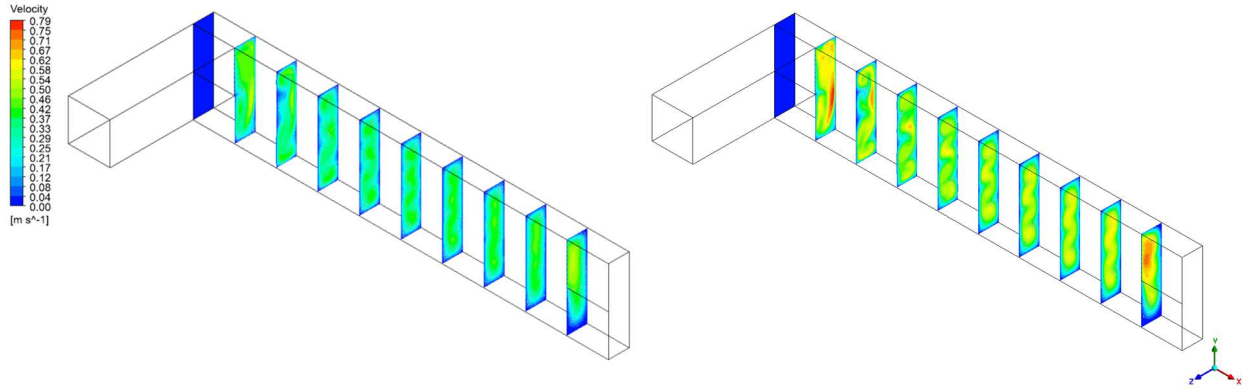

(a) *(b)*

Figure 8- Velocity contours for Re=250 (a) and 350 (b).

The flow characteristics do not change significantly along the length of the main channel and the fluid mixing is more homogeneous at the centre. However, the steep expansion from the inlet channel to the main chamber has been shown to increase flow rotation in that area, with the same happening at the outlet region of the cell. Secondary flow is promoted in the form of Dean vortices, which enhance mixing in the DeanCell and mass transfer to the reactor walls.

Other flow maps are shown in Appendix B, in the form of velocity path lines.

4.2 Tracer Simulations

To further complete the flow characterization study, transient simulations were performed to assess the evolution of the hydrodynamics inside the DeanCell over time. In particular, tracer injection experiments and the monitoring of the evolution of the NH_3 concentration at the outlet of the cell were carried out for the RTD study.

Contour maps of the flow inside the cell, created with CFD-Post and present in Appendix C, show the presence of stagnant zones inside the cell. To minimise this problem, a different configuration of the DeanCell was created, and the RTD curve was computed and compared with the original configuration, to determine the influence of the outlet channel position in the residence time of the fluid elements.

Figure 9 shows the new geometry (Geo2) and a detailed view of the outlet channel of the generated mesh, which was shifted to a lower y-position. A steady-state flow simulation ($\mathrm{Re} = 250$) was first performed to check that velocity profiles and flow patterns were kept accurately throughout the reactor.

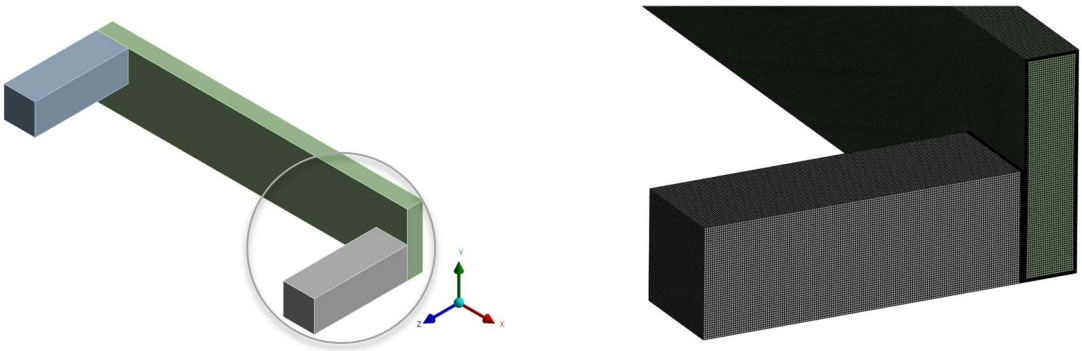

(a) *(b)*

Figure 9- Geometry (a) and generated mesh (b) for the new Geo2 cell.

Figure 10 represents the $F(\theta)$ curve for the flow inside the DeanCell, for the first (Geo1) and second (Geo2) geometry, and the PFR curve, which corresponds to the ideal behaviour of a Plug-Flow Reactor.

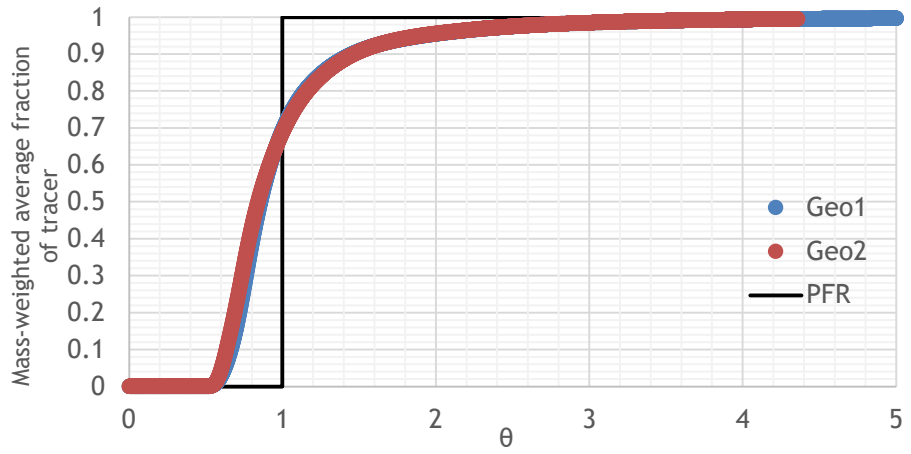

Figure 10- $F(\theta)$ curve for Geo1 and Geo2.

For further analysis of the hydrodynamics of the system, the RTD curve, $E(\theta)$, shown in Figure 11, was obtained from the derivative of the $F(\theta)$ curve.

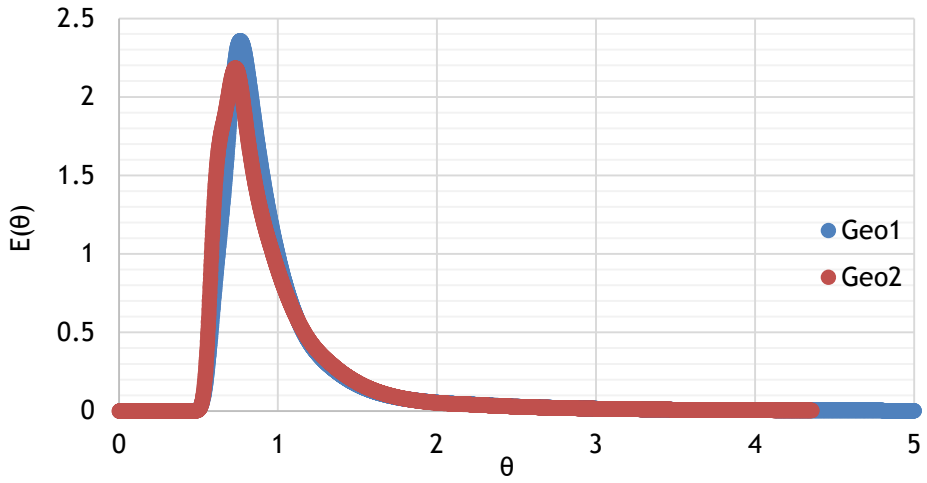

Figure 11- RTD Curve for Geo1 and Geo2.

The $E(\theta)$ peak shows that most elements leave the reactor before the reactor's passage time: $\theta = 1$. The main flow path provides a shortcut to the flow that is not too pronounced, probably due to the higher velocities in the reactor. The absence of additional peaks indicates that no significant recirculation zones or bypasses are present and that the Dean vortices are promoting good mass transfer in the cell.

The narrow RTD curve indicates the uniformity of the residence time across all fluid elements, as well as good fluid homogenization inside the reactor.

Table 2 compares the difference between the residence time, τ, calculated through the ratio between the volume of the reactor and the considered flow rate, and the mean residence time, $\bar{t_r}$, estimated through equation 20, for the two geometries.

Table 2- RTD parameter analysis.

Re	τ /s	$\bar{t}_r$ /s	$\bar{t}_r/\tau$	V_d (%)
Geo 1	0.06388	0.06339	0.992	0.77
Geo 2	0.06388	0.06213	0.973	2.70

When comparing the RTD curve for both geometries, through Figure 11, the maximum peak time of Geo1 is higher than the one of Geo2, meaning that the dead volumes are less significant for the first geometry. This is confirmed through the calculation of the dead volume inside the cell, which showed higher relevance in the second case.

Sketches of Figure 12 show the areas within the DeanCell in which the mass fraction of tracer is below 0.5, at the final time step, as a way to analyse possible stagnant or lower velocity zones.

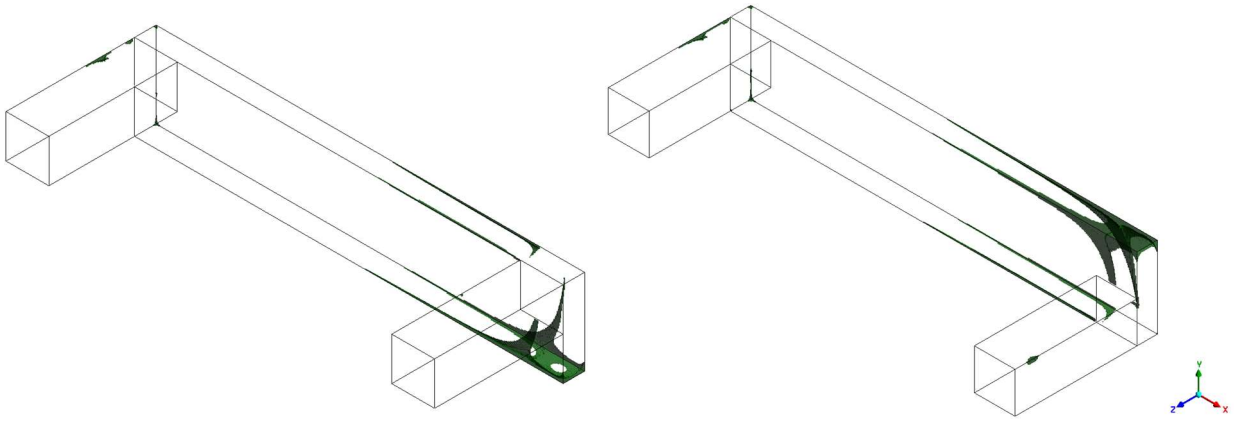

Figure 12- Illustration of the areas of the DeanCell with a tracer mass fraction below 0.5.

For both geometries, the areas with lower fluid velocity and thus smaller tracer concentrations are opposite to the step. The design of a new geometry showed not to be very effective in increasing mixing in the cell, and so the first geometry was kept at the optimum base case geometry for following simulations.

In this RTD study, the simulations were only performed for a Re number of 250. Due to the small dimensions of the cell, the flow regime is laminar but forms a complex secondary flow pattern. This flow needs to be addressed at different Reynolds numbers because the evolution of its patterns will create different contact times with the walls. The prismatic geometry of the DeanCell promotes the creation of Dean vortices, that increase the contact with the walls, which could shift the operation of the cell to the chemical regime, i.e. not limited by diffusional mass transport. On the other hand, increasing the Reynolds number decreases the residence time of the overall flow, what could lead to an increase in mass fraction gradients and thus

lower conversion of reactants. Therefore, the effect of the Reynolds number is a trade-off between the increase on vortex dynamics, and thus, convective transport, and the decrease of time for diffusive mass transfer. So, this parameter should be addressed in the range of operation for this cell (100 to 1000).

4.3 Mass Transfer Results

One of the main objectives of this work relates to the assessment of the mass transfer limitations that the DeanCell geometry imposes on the ammonia production at the outlet of the cell. Mass transfer simulations were performed to establish the maximum limits for mass transfer within the unit-cell.

4.3.1 Mesh Validation

Hydrodynamics and mass transfer studies occur at different scales. While the mass transfer is evaluated mainly at boundary layers and across interfaces, hydrodynamics is characterised at a larger scale (vortices). A typical scale for mass transfer is the Batchelor scale, λ_B, that is related to the hydrodynamic scale, λ_K, by

$$\lambda_B = \lambda_K/\sqrt{Sc} \tag{21}$$

with the Schmidt number (*Sc*) for liquids generally on the order of magnitude 1000 ($Sc \propto 10^3$). Therefore, two mesh validation studies should be performed for the study of these two phenomena.

To better assess the influence of mesh refinement in mass transfer evaluation, the grid was again validated, and a new mesh was generated, considering that the catalyst is immobilised on the interior and exterior walls of the main body, as highlighted in Figure 13.

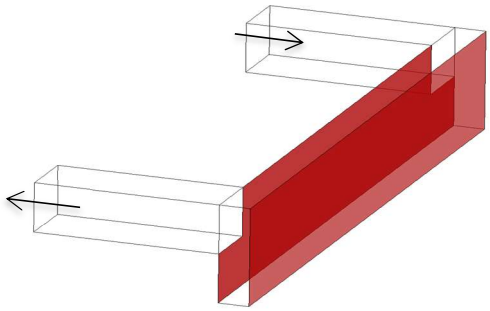

Figure 13- Highlighted view of the walls where the catalyst is immobilised.

Inflation was only defined on these two body surfaces to more accurately capture the boundary layer region, where the diffusion of NH_3 from the catalyst to the bulk occurs. The mesh element

size was kept constant and equal to 2 x10^{-5} m. The mesh validation was carried out in two phases: liquid and gas phase simulation.

- **Liquid Phase Simulations**

The first study consisted of the assessment of the variation of the Sh number with the first layer thickness of the inflation boundary. If no significant change is observed, mesh independence is guaranteed.

Seven grids with different first layer thicknesses ($\Delta x_{\,first\ layer}$) were generated. The number of layers in the inflation boundary varied and was approximated according to

$$\Delta x = \Delta x_{\,\text{first layer}}\ r^{\,n} \tag{22}$$

where *n* is the number of layers and *r* is the growth rate.

The Coupled Scheme was chosen for pressure-velocity coupling, and all other methods for spatial discretization were set. The mesh validation was performed for a $\mathrm{Re} = 250$.

Figure 14 shows the variation of the Sh number with the increase in the thickness of the boundary's first layer.

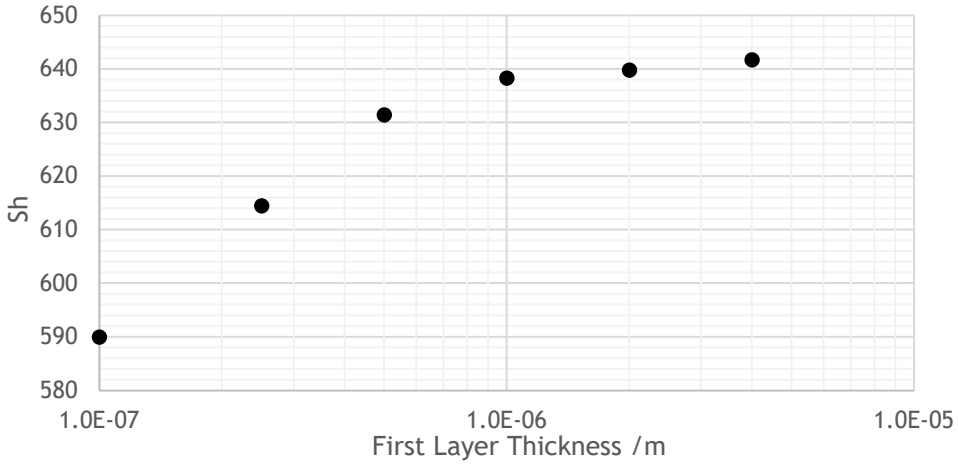

Figure 14- Sh number variation with thickness of the first layer of the mesh (liquid phase).

As predicted, for highly refined meshes, the calculations performed within the control volumes are optimised, meaning the value of Sh depends on the grid size. Results show that more refined meshes better describe ammonia diffusion through the reactor. Therefore, the smaller the boundary element size, the more accurately the mass transfer phenomenon is defined.

Besides, in this liquid flow, where the Sc number is around 1000, the Batchelor scale is approximately 30 times smaller than the hydrodynamic scale. This means that the length of each grid element should be refined over 30 times to improve the mesh resolution for the numerical simulations. While this gives a more accurate solution, it requires, however, extreme computational power.

Figure 15 shows the comparison results between the CFD data and an estimated solution calculated through Richardson's Extrapolation method (Equation 9), which was taken as the most accurate value for convergence. The extrapolated value was calculated based on three meshes with first layer thicknesses of $1x10^{-6}$ m, $2x10^{-6}$ m and $4x10^{-6}$ m, in order to keep the ratios of the inflated layer equal to 2.

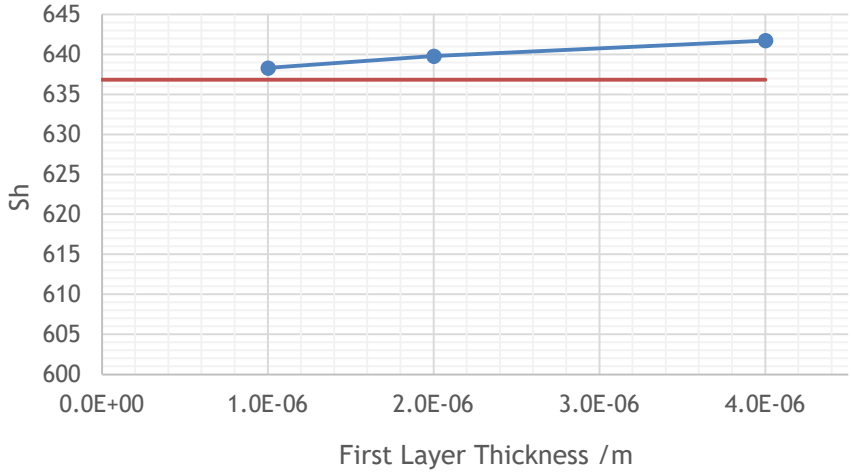

Figure 15- Richardson Extrapolation method for the study of the inflation layer size.

The Sh number for a mesh with a first layer thickness of $1x10^{-6}$ m was only 0.2% away from the Richardson extrapolated value and thus can be an excellent approximation to the true solution. It was also chosen in preference to the other two more refined meshes, due to significantly smaller computation time.

- **Gas Phase Simulations**

Because of the low yield for ammonia production in liquid phase at atmospheric pressure, due to the low solubility of N_2 in water, the flow inside the reactor was also simulated in a gaseous phase.

The grid independence test was repeated. A new mixture of NH_3 (g) and water vapour is set in ANSYS Fluent. The mass diffusion coefficient was set as 1×10^{-5} $m^2 \cdot s^{-1}$, which is the characteristic value for gases, and the mixture's physical properties can be approximated to the density and viscosity of H_2O (g): ρ = 0.554 $kg \cdot m^{-3}$ and μ = 1.34 $x10^{-5}$ $kg \cdot m^{-1} \cdot s^{-1}$.

To ensure the same ratio between inertial and viscous forces (i.e., keeping the same Re of 250) as the one of the liquid phase simulations, the injection velocity was altered to 6 $m \cdot s^{-1}$ for the gas-phase validation, according to Equation 14.

Once again, no reaction is modelled in the walls. For sake of comparison with the previous case, the NH_3 mass fraction at the walls is set at the same limit concentration defined for the liquid phase. This means that the maximum concentration of NH_3 that would occur in the walls if there were no mass transfer or chemical reaction limitations is defined. While this does not

represent a true physical case, as the quantity of gaseous NH_3 in water vapour is higher than in liquid, it aims only to verify the model and study how the phase of the fluid influences the transport of ammonia throughout the cell.

Figure 16 shows the Sh number for different sizes of the first inflated layer of the boundary region.

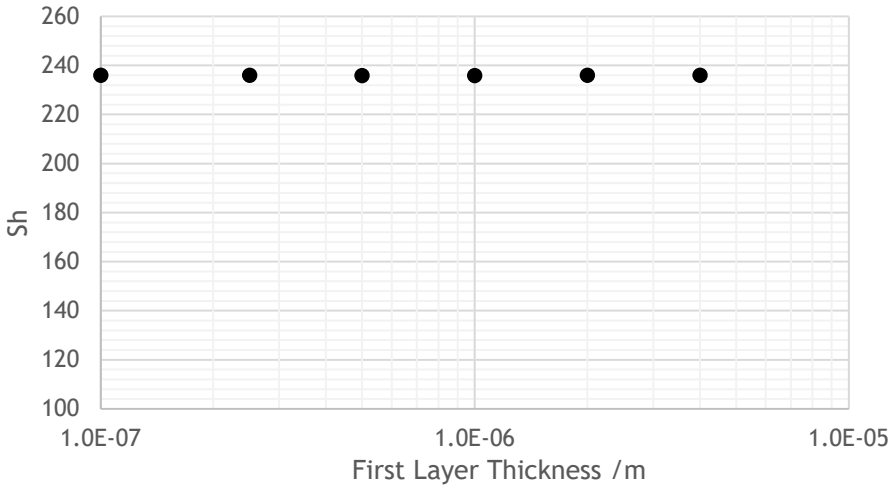

Figure 16- Sh number variation with the thickness of the first layer of the mesh (gas phase).

Contrarily to liquid phase simulations, the thickness of the first layer shows no influence on the mass transfer phenomena at the DeanCell, as illustrated in Figure 16. As the diffusivity in gases is 10^4 higher than in liquids, the profiles for the concentration gradients between the catalytic plate and the bulk are much more abrupt. This might explain why mesh refinement is not as important in these types of simulations, as less refined meshes are still able to fully describe these gradients. In addition, as the Sc number for gases is lower and closer to 1, it means that diffusion and hydrodynamics occur at similar scales, unlike liquids. This makes it easier to describe both phenomena with less refined grids and less computational requirements.

4.3.2 Main Results

To study the influence of the catalyst position on the overall efficiency, different catalytic immobilisation configurations are studied. The NH_3 diffusion from the catalyst surface to the fluid phase is monitored through a report of the ammonia concentration at the outlet.

Table 3 shows different possible combinations for the immobilised surfaces, with respect to the named selections illustrated in Figure 6, and the corresponding values for the mass transfer coefficient and the Sh number, that quantitively characterise mass transfer from the catalytic plate to the fluid phase.

Table 3- Values of k and Sh for the catalyst immobilisation study.

v_{in} / m·s^{-1}	Catalyst immobilisation	C_{out} /M	k / m·s^{-1}	Sh
0.25	top wall + interior wall	1.54 x 10^{-5}	1.23 x 10^{-4}	530
	top wall + exterior wall	2.32 x 10^{-5}	1.72 x 10^{-4}	**740**
	bottom wall + interior wall	1.41 x 10^{-5}	1.12 x 10^{-4}	485
	bottom wall + exterior wall	2.20 x 10^{-5}	1.62 x 10^{-4}	699
	interior wall + exterior wall	3.06 x 10^{-5}	1.49 x 10^{-4}	645
	top wall + bottom wall	6.76 x 10^{-6}	1.23 x 10^{-4}	532
0.35	top wall + interior wall	1.64 x 10^{-5}	1.84 x 10^{-4}	793
	top wall + exterior wall	2.13 x 10^{-5}	2.20 x 10^{-4}	**951**
	bottom wall + interior wall	1.48 x 10^{-5}	1.65 x 10^{-4}	713
	bottom wall + exterior wall	1.90 x 10^{-5}	1.96 x 10^{-4}	847
	interior wall + exterior wall	2.87 x 10^{-5}	1.96 x 10^{-4}	847
	top wall + bottom wall	6.75 x 10^{-6}	1.72 x 10^{-4}	744

For both Re numbers, the highest concentration value was reported for the case of the catalyst immobilisation on the internal and external walls of the DeanCell. This coincides with the case of the highest superficial area, which can explain the higher yields reported at the outlet. However, these are not the cases of higher flux. In fact, these concentration values were computed through area-weighted average surface integrals, meaning that different flow patterns and product distribution inside the cell influence the reported average value in the outlet face.

The higher Sh numbers for $\mathrm{Re} = 350$ confirm the influence that higher velocities of the fluid phase have in the mass transfer phenomena.

Figure 17 shows the different contour maps for the diffusion of ammonia inside the DeanCell (for $\mathrm{Re} = 350$), for different catalyst immobilisation configurations, for a side view of the outlet channel. The schematic representations of the DeanCell in Figure 17 highlight, in red, the walls where the catalyst is immobilized: top and exterior walls, for the first case, and bottom and exterior walls, for the second.

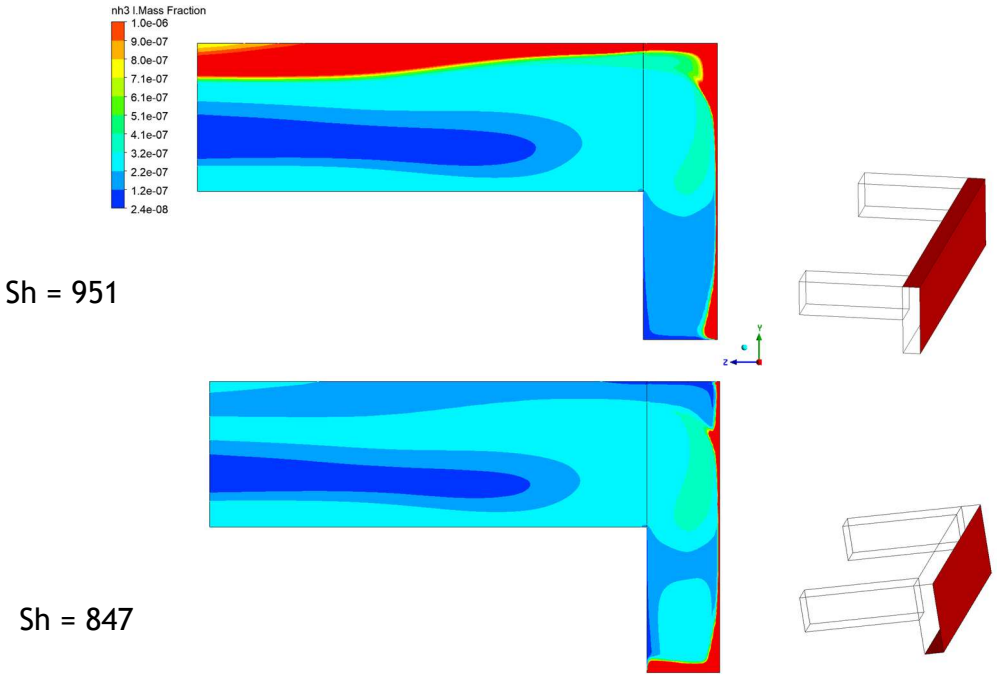

Figure 17- Mass fraction contour maps for two different configurations, for $Re = 350$.

The case of the higher Sh number $(\mathrm{Sh} = 951)$ corresponds to the one on the top of Figure 17. Even though the diffusion through the outlet channel is more more significant in the top case, the ammonia transport through the DeanCell is slow and uneven, and the NH_3 concentrations are low in the entire cell, except close to the catalytic walls, where they reach their highest values.

Contour maps of the NH_3 mass fraction at the outlet face allow a better understanding of how ammonia travels inside the cell. The analysis of the vorticity along the main chamber, in the region close to the walls, enables to understand how the vortices influence the dispersion of mass.

Figure 18 illustrates the evolution of the NH_3 mass fraction for the same two configurations at the top.

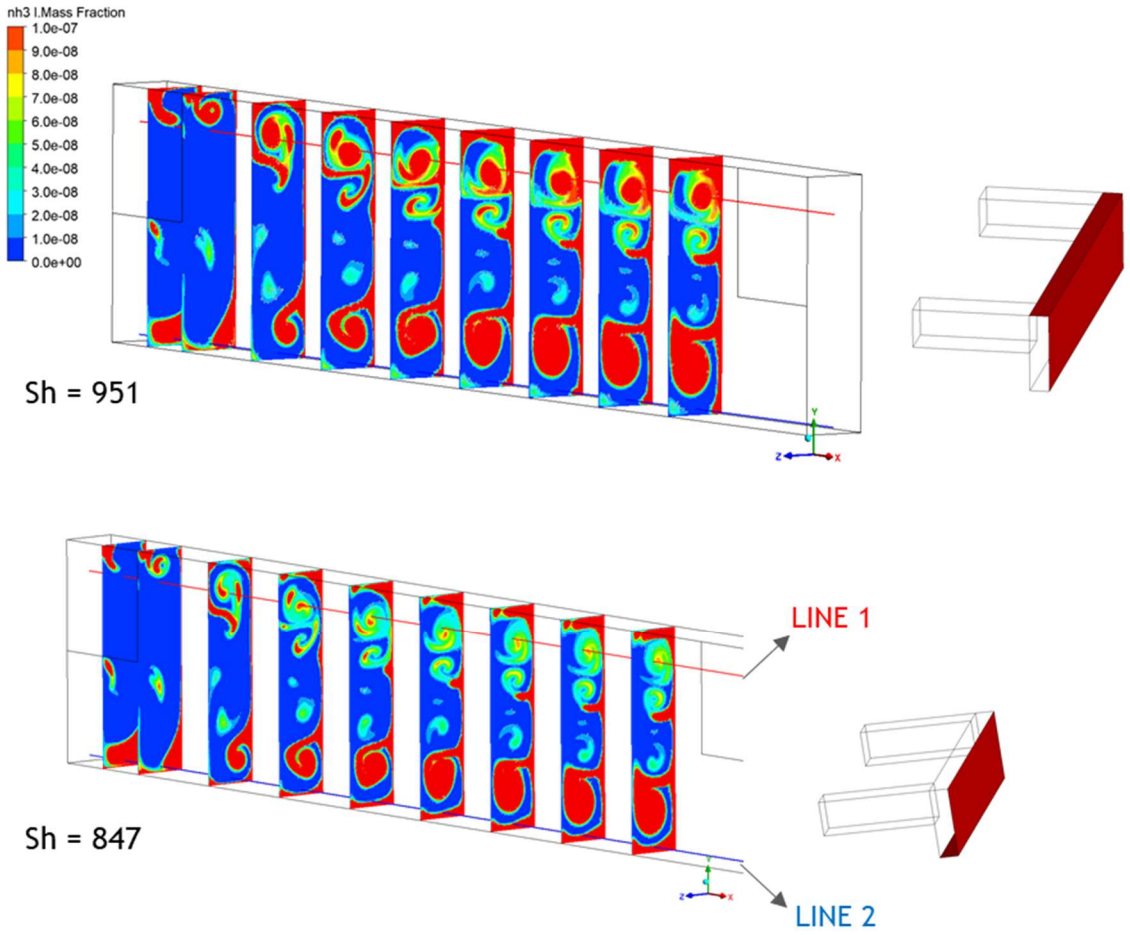

Figure 18- Evolution of ammonia mass fraction along the cell for two different configurations, for $Re = 350$

In terms of the catalyst configuration inside the cell, the best simulated case is the immobilisation on the top and exterior walls. Despite showing similar flow patterns, the vortices close to the top wall promote a wider dispersion of mass on the case of $\mathrm{Sh} = 951$, which is confirmed in the contour map of Figure 17. Near the bottom wall, even though the mass fraction is higher, the vortices are less expanded and promote accumulation, not enabling the recirculation and affecting the convective transport of ammonia to the outlet.

A vorticity plot was traced along two parallel lines, Line 1 and Line 2 (illustrated in Figure 18), close to the top and bottom walls of the body, respectively. This chart is shown in Figure 19.

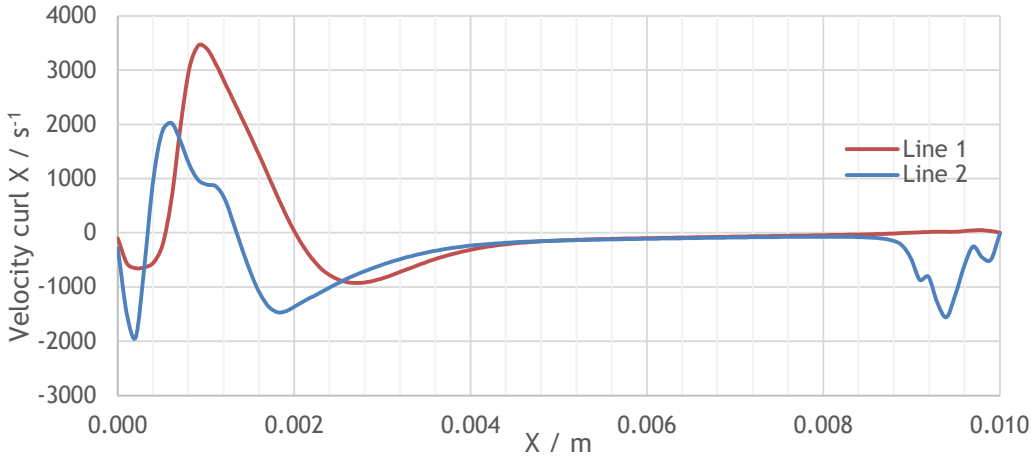

Figure 19- Vorticity plot along the x-direction in the main chamber, for the flow at Re= 350.

The vorticity is significantly higher near the top wall, specifically at the entrance of the main body ($x = 0.001$ m). The configurations where the catalyst is located in an area with higher vorticity present an increased velocity gradient in the walls. This increases the mass transfer from the catalyst to the bulk, and promotes a better convective transport, leading to higher Sherwood numbers. In the bottom case ($\mathrm{Sh} = 847$), the catalyst is immobilised in the bottom wall, close to an area with lower vorticity, meaning that the limitations to the mass transfer are more notable and promote a decrease on the ammonia flux at the end of the cell.

4.4 Reaction Modelling

To analyse the effects of micromixing (diffusion and convection) on the chemical reaction, the gas-phase reaction between H_2 and N_2 was modelled as a wall surface reaction in ANSYS Fluent.

The coupled scheme was used for pressure-velocity coupling and the third order MUSCL for the NH_3 equation was used for special discretization. The residuals were set to 10^{-6} as the convergence criteria for all equations, including the energy.

As the experimental simulations are still under development and being performed in liquid phase, no valid kinetic parameters could be used in the setup of the simulation cases. The values of the pre-exponential factor, *A*, and the activation energy, E_a, are reported in Table 4. The estimated value for E_a is as an acceptable value for the use of g-C_3N_4 as a catalyst and agrees with other values reported in studies of this particular reaction (Rouwenhorst et al. 2019).

The simulation was performed at steady state, at atmospheric pressure, with adiabatic conditions at the walls. Table 4 summarises the inputs and outputs of the reaction simulation.

Table 4- Fluent Data for the simulation of the ammonia synthesis reaction.

Simulation Inputs		
Reynolds Number		250
Inlet Mole Fraction	N_2	0.25
	H_2	0.75
A / mol·m^{-2}·s^{-1}		1 x 10^{15}
E_a / kJ·mol^{-1}		90
Simulation Outputs		
$C_{NH3,\ outlet}$ / kmol·m^{-3}		2.45 x 10^{-2}
k / m·s^{-1}		0.244
Sh		244
N_2 conversion, X_{N2} / %		60

Graphic contours are used to visualise the diffusion of the produced NH_3, to better understand the evolution of the flow inside the DeanCell. Figure 20 shows the mole fraction contours of ammonia through the DeanCell and on a section plane in the middle of the main channel.

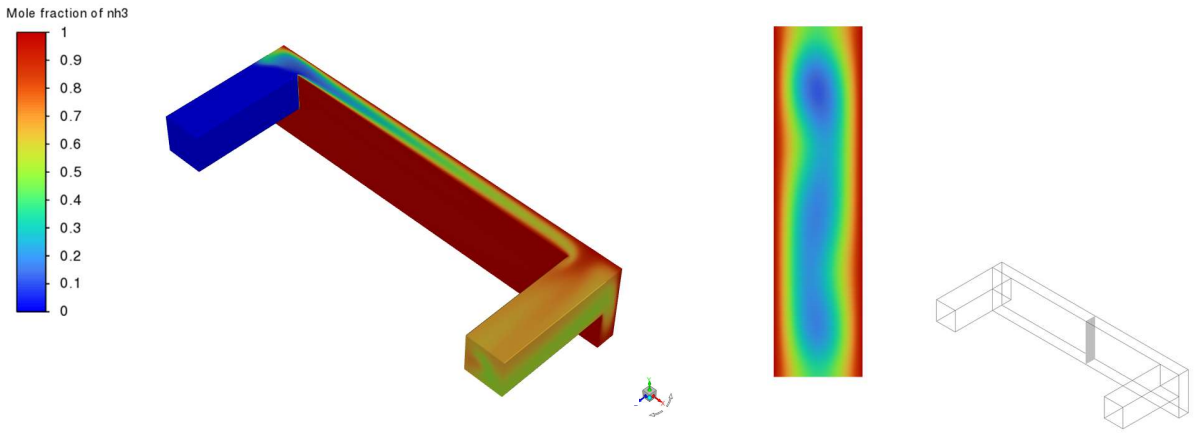

Figure 20- Contour maps of ammonia in the DeanCell, at 1 bar.

As expected, since the catalyst is immobilised at the main chambers' walls, the reaction only starts in that area of the cell. The NH_3 concentration increases along the length of the DeanCell, having its higher value closer to the walls. In the vortices area, there is an increased recirculation of the gas phase and the ammonia fraction in the centre is lower than near the walls.

Despite showing high conversion values, the product is retrieved at the outlet at atmospheric pressure. However, to be used as an effective energy carrier and to reduce the cost of storage

and transportation, ammonia should be liquified. Unlike liquid hydrogen, which shows a low volumetric energy density of 5.6 $MJ \cdot L^{-1}$ at 700 bar, liquid ammonia shows a much higher value of 15.6 $MJ \cdot L^{-1}$, at a pressure of only 10 bar (Valera-Medina et al. 2018).

For this reason, the reaction was also simulated for a pressure of 11 bar. Figure 21 shows the mole fraction of NH_3 along the DeanCell, for that operating condition.

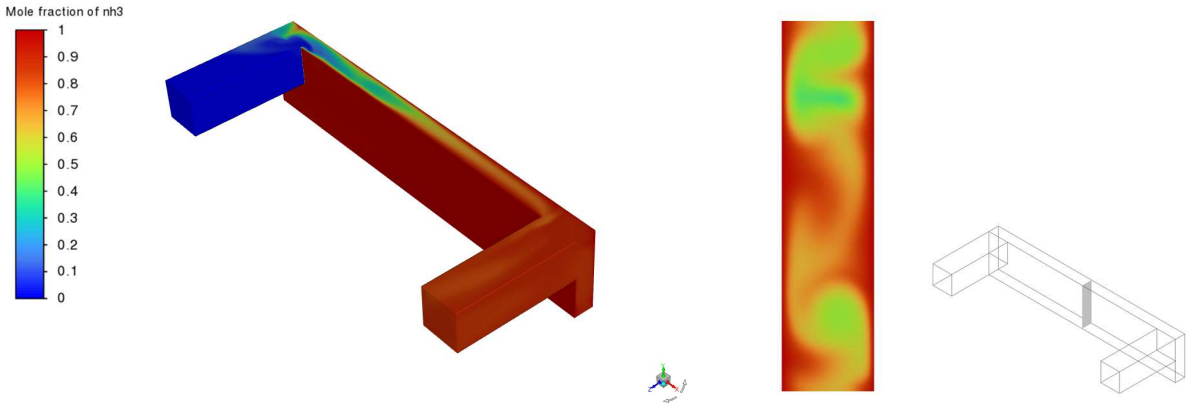

Figure 21- Contour maps of ammonia in the DeanCell, at 11 bar.

Through the analysis of Figures 20 and 21, it is possible to verify that the dispersion of mass is more uniform at higher pressures, and NH_3 starts being produced at earlier axial positions inside the cell (with a final N_2 conversion of 87% at the outlet), compared to the case of 1 bar. The vortices increase the contact time between the fluid elements, enhancing the mixing and the reaction yield. Besides, increasing the pressure favours the synthesis reaction, which adds to an increase in the mole fraction at the outlet.

However, at both pressures of 1 and 11 bar, the maximum temperatures reached by the reaction are close to 1000 ºC and 3000 ºC, respectively, which are too high to allow the use of g-C_3N_4 as the reaction's catalyst, as it can only handle temperatures up to 500°C.

To minimise this problem, thermal conditions are applied to the walls as boundary conditions.

As a first step, radiative flux was modelled across the walls of the DeanCell to simulate heat transfer. The material of the top wall of the cell was considered as silica, with an emissivity, ε, of 0.79, while the other walls were modelled as stainless-steel walls ($\varepsilon = 0.4$). The thickness of all walls was defined as 0.02 m, to support the reactor and withstand larger temperatures.

These simulations were performed using the same methods as in the case of the adiabatic walls and were run for both pressures of 1 bar and 11 bar.

At atmospheric pressure, the nitrogen conversion was registered as 63%, superior in 3% to the conversion of the adiabatic case. However, the cooling term that was added to the model, by considering flux through the walls, enabled a decrease in the maximum temperature (reported at the entrance of the outlet channel) from 959°C to 772°C.

The wall flux contours of Figure 22 confirm the heat transfer across the walls of the main chamber.

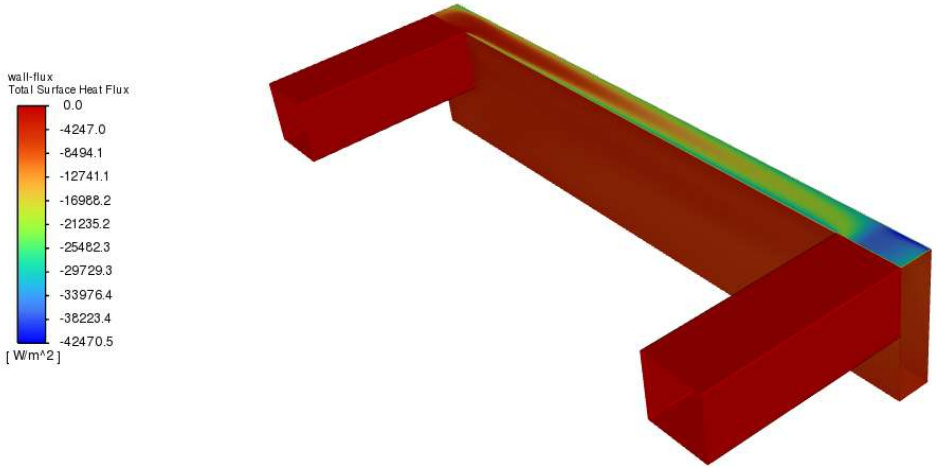

Figure 22- Wall heat flux contours for the DeanCell.

As predicted, this phenomenon shows an increased effect on the top wall, which has greater emissivity values. For improved heat transfer under the form of radiation, the material of the cell could ideally be modelled as acrylic, which shows emissivity values up to 0.95, depending on the film thickness. However, the glass transition temperature of this type of material is low (around 100 ºC), making it impossible to be used in a cell with no cooling of the walls.

To deepen the understanding of how the modelling of heat flux through the walls affects the overall temperature of the DeanCell, forced convection was also simulated. A heat transfer coefficient of 1000 $W \cdot m^{-2} \cdot K^{-1}$ was defined at the walls, being in the range of typical values for forced convection of gases. However, by using other cooling agents for forced convection, such as water or boiling water, the heat transfer coefficient can be increased up to 10^4 or 10^6, to promote much higher heat transfer rates (Kakaç et al. 2005).

The same parameters were evaluated for all simulations, and Table 5 summarises the outputs for all cases.

Table 5- Summary of simulation outputs for all four reaction simulations.

Thermal Condition	P /bar	X_{N2} /%	Sh	Average Temperature/ ºC	Maximum Temperature / ºC
Adiabatic	1	60	244	597	959
	11	87	1087	1038	3208
Radiation	1	63	274	522	772
	11	79	616	967	2700
Forced Convection	1	61	247	149	527
	11	72	413	721	2442

When working at 11 bar, the synthesis reaction is favoured and the nitrogen conversion is superior. However, as the reaction is exothermic, a further extent of the reaction is followed by a temperature increase, which is negative from the system's operation perspective. Despite significantly lowering the temperature, the introduction of the cooling term on the walls is not sufficient, at 11 bar, to enable the use of g-C_3N_4 as the catalyst, since this material is stable only up to 500 ºC (Lima et al. 2017).

At 1 bar, the temperatures inside the cell are lower and more favourable from the cell's operation point of view. Yet, the conversion and, especially, the values of the Sh number are significantly inferior, meaning the mass transfer inside the cell is not as high and the limitations imposed by the diffusion phenomena are more intense.

It seems, however, that working at atmospheric pressure and under forced convection is the most feasible case, as the average temperatures are the closest to the stabilization temperature of the catalyst. The model should be further verified for other heat transfer coefficients and consider more efficient ways to cool the reactor, such as, for example, adding an adjacent prismatic chamber with baffles with water flow, to lower the operating temperature (Costa et al. 2017).

5 Process Integration: ASPEN Simulations

Model verification ensures the accuracy of the produced model and the data it generates. This chapter presents the development of a simulation model through ASPEN Software for process integration of the simulated mesostructured photocatalytic reactor. The data generated through CFD on the design and operation of the reactor was used for a complete process simulation.

5.1 DeanCell: process integration and techno-economic analysis

The process flow diagram for the photocatalytic process was built based on the Haber-Bosch process, which was later optimised on an energy basis. The composition and operating conditions of the feed streams and other process units were changed to the typical values of the photocatalytic process. The process flow diagram that models the conventional Haber-Bosch process can be found in Appendix D, and was built from a template provided by AspenTech.

Similarly to the Haber-Bosch model, the RKS-BM (Redlich-Kwong-Soave-Boston-Mathias) property method was chosen for this process simulation. Its use is recommended for gas-processing plants and literature shows accurate results for a wide range of temperature and pressure, for hydrocarbons and light gases. However, specific conditions were previously simulated and the model was shown to accurately describe the physical properties of ammonia.

Figure 23 illustrates the final designed flowsheet of the process.

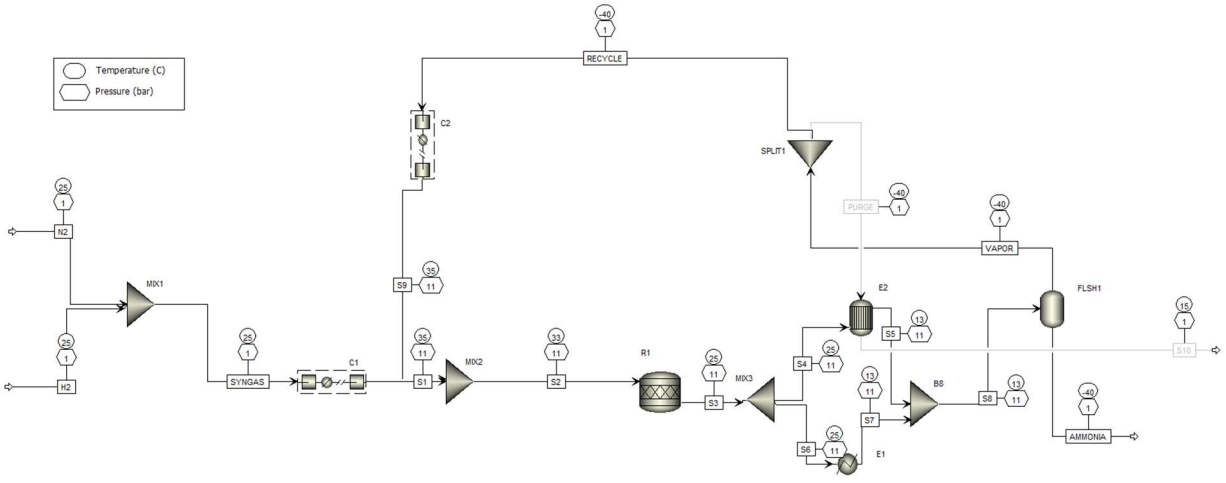

Figure 23- Process Flow Diagram for the simulation of the photocatalytic process.

According to the ammonia synthesis reaction, and following the CFD simulations, two streams of N_2 and H_2, of 1750 mol·hr^{-1} and 5250 mol·hr^{-1}, respectively, and on a stoichiometric ratio of 1:3, were fed to the system, at 25ºC and 1 bar. These feed streams were mixed before entering

a compression system, that set the final discharge pressure at 11 bar. This compressed stream is mixed with a compressed recycle loop, that aims to recover unreacted gases.

Multi-stage compressors (C1 and C2) were used to model the gas compression of feed and recycling streams. This multi-stage compression was used instead of only one compression stage (as presented for the Haber-Bosch process), to avoid high gas temperatures at the compressor outlet and reduce power consumption. The compression ratio was kept equal in each stage of the compressing unit and the number of stages, j, was set as 3, according to the following equation

$$\left(\frac{P_2}{P_1}\right)^{1/j} < 3 \tag{23}$$

where P_1 and P_2 are the inlet and discharge pressures, equal to 1 and 11 bar, respectively.

Both compressing blocks, C1 and C2, have inter and aftercoolers to remove generated heat during gas compression. This cooling is done using a cooling water utility that is available at 20°C and leaves the process at 25°C. A pressure drop of 0.15 bar was considered in each water cooler for vapour streams. The minimum temperature difference (ΔT_{min}) was assumed as 5°C, which allowed to set the discharge temperature of the intercoolers as 25°C and thus suppress the heat exchanger upstream of the reactor. The reactor operating temperature was fixed at 25°C, to enable the removal of the heat duty generated in the reaction using cooling water. This suppressed the need for refrigeration in R1, so the outlet temperature of gas streams leaving the aftercoolers was defined as 35°C.

Therefore, the stream is mixed with the recycled loop and enters the reactor at 33ºC, where an average N_2 conversion of 60% was defined, through data from CFD simulations.

As clearly stated through the reaction's stoichiometry (Equation 1), increasing the pressure of the process favours the reaction, thus increasing ammonia production. Besides, if the pressure inside R1 is kept at 11 bar, the NH_3 liquefication can be done at higher temperatures, reducing energy consumption in the E1 chiller, downstream of the reactor.

An ammonia production stream of 42.5 tonne·hr^{-1} was obtained at the liquid phase that exits the bottom of the flash unit (FLSH1), at -40ºC and 1 bar. The vapour stream, that is redirected to the recycle loop, is split into two, with 10% of this stream exiting the process as a purge. Direct process heat integration was done in E2, using the purge stream, which, due to its low temperature, allowed to reduce the refrigerant use in E1.

To analyse the operating expenses (OPEX), a mapping of different cost elements was performed, mainly: electricity and the cooling water and refrigerant consumption. Table 6 summarises this analysis and presents the considered unit costs for each utility. The OPEX cost was obtained by dividing the total costs by the mass flow rate of NH_3 produced.

Table 6- OPEX Analysis of the photocatalytic process.

Operational Expense	Total Requirement / kW	Unit Costs / $\$\cdot kWh^{-1}$	Total Costs / $\$\cdot hr^{-1}$
Cooling Water	8.22×10^4	0.0013	105
Refrigerant	2.36×10^4	0.016	377
Electricity	4.49×10^4	0.12	5386
Total Cost ($\$\cdot hr^{-1}$)			5868
Total electricity consumption (GJ· (tonne produced NH_3)$^{-1}$)			3.8
Total OPEX cost ($\$\cdot$ (tonne produced NH_3)$^{-1}$)			138

As clearly stated in Table 6 above, the electricity requirement associated with gas compression accounts for the larger share of the operating costs. Cooling water was used on the reactor and all coolers of the multi-stage compression. The cooling of the reactor unit represents over 50% of the total duty concerning cooling water expenses.

The reported values in the literature for energy demand and costs of ammonia plants are primarily dependent on the source of hydrogen that is supplied as the feed stream, representing over 90% of the overall costs of renewable production. Recent reports claim that, in the case of renewable ammonia plants, only approximately 10% of the costs are associated with N_2 separation and the ammonia synthesis loop (IRENA and AEA 2022). However, the simulations performed within the scope of this work aimed only to analyse NH_3 production expenses and thus cannot be directly compared to the overall given values.

Carbon mitigation incentives and high competition in the renewable ammonia production area are expected to make the photocatalytic process more economically competitive. The reported values for production costs of new renewable ammonia plants revolve around 720-1400$/tonne of NH_3, as illustrated in Figure 24.

Assuming, for comparative purposes, that the total OPEX calculated accounts for 10% of the overall expenses (and neglecting the cost of the N_2 purification step), the cost of the photocatalytic process would be close to 1380$ per tonne of ammonia and running around 38 $GJ\cdot tonne^{-1}$. Again, this value is only an estimate and does not consider the cooling water and refrigerant consumption, but, as seen through the OPEX analysis, this value is barely accountable when compared to the energy consumption in the compression equipment.

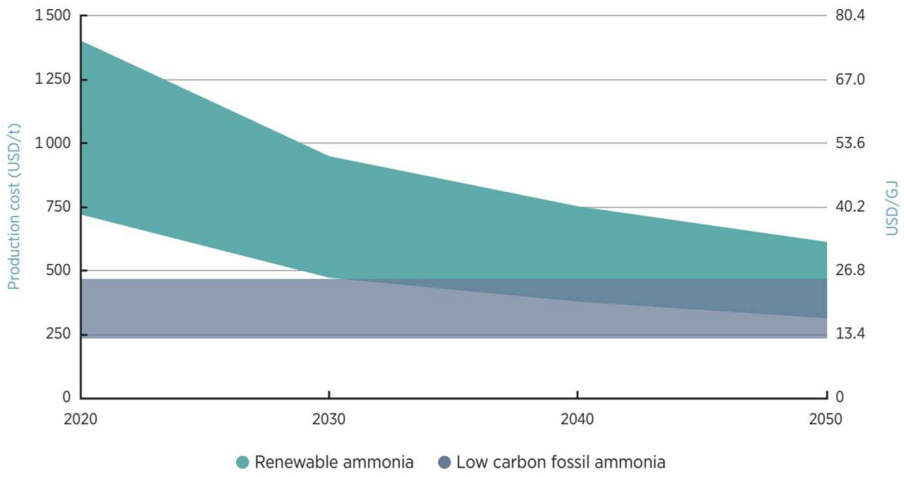

Figure 24- Current and future production costs of renewable ammonia and low-carbon fossil ammonia. Retrieved from IRENA and AEA (2022).

Even though only a rough estimate was performed, and further simulations should more accurately address the costs of H_2 production, N_2 purification and other possible operating costs, the process achieves similarly good results when compared to the trend for other renewable ammonia plants.

6 Conclusions

This work reports a study on the development of a mesostructured photoreactor to be used in immobilised catalytic systems for application in green-ammonia synthesis. A unitary element of the structured reactor is designed and optimised through a numerical approach using CFD tools.

Hydrodynamic studies evaluated the fluid behaviour and the mixing patterns inside the reactor, for two different Reynolds numbers (250 and 350). Fully developed parabolic velocity profiles were established at the inlet channel for all simulations, through a user-defined function. It was determined that the step perturbation and overall prismatic geometry of the cell promoted secondary rotational flow- Dean flow-, boosting contact between the fluid elements and increasing the mixing degree. Furthermore, the residence time distribution curve suggests good fluid homogenization and dispersion of mass in the cell.

Mass transfer limitations within the DeanCell were quantitively assessed by the calculation of Sherwood numbers, with the highest reported value being 951 for catalyst immobilisation on the top and external walls. CFD results show that ammonia diffusion is not significantly affected by the localization of the catalytic material, but the vorticity close to the walls increases the velocity gradient and the mass transfer.

The gas phase reaction between N_2 and H_2 was modelled as a surface reaction on the interior and exterior walls of the main channel. The reported temperatures reached by the exothermic reaction are too high to allow the use of g-C_3N_4 as the photocatalyst, which raises the need for the cooling of the reactor, either through radiative wall heat flux or forced convection. Future studies should further evaluate this issue.

CFD data was integrated in a complete process simulation, using the modelled photocatalytic reactor. The reactor operating conditions and kinetics were not validated, so the ASPEN simulations were performed only as a way to verify the model. Thus, to correctly conclude on the limiting step process, the ammonia production values reported through the simulations should be compared to the experimental results for the reaction kinetics.

7 Assessment of the work done

7.1 Objectives Achieved and Future Work

The main objective of this work was to build a CFD model to study the behaviour of a multifunctional mesostructured immobilised photoreactor for NH_3 production.

The configuration of the unitary element of the structured reactor was optimised through the simulation data and it showed good results in enhancing the mixing quality of the fluid phase. The prismatic geometry of the cell, more specifically, the step structure drawn at the end of the distributor channels, promotes increased flow rotation through Dean vortices, which is favourable in any reaction medium.

In future work, the validation of the model with experimental data will allow a deeper understanding of the production limits of the DeanCell. It is important to recall that the reaction modelling simulations were performed without validated kinetic parameters, and so can only be seen as a good estimate of the behaviour of the cell, under the design conditions. A more in-depth photocatalytic model should also aim to simulate the radiation field inside the DeanCell.

8 References

Adesina, A. A. (2004). "Industrial exploitation of photocatalysis: progress, perspectives and prospects." Catalysis Surveys from Asia **8**(4): 265-273.

Ahmed, S., M. G. Rasul, M. A. Sattar and M. I. Jahirul (2022). "Phenol degradation of waste and stormwater on a flat plate photocatalytic reactor with TiO_2 on glass slide: An experimental and modelling investigation." Journal of Water Process Engineering **47**: 102769.

Amaral, R. N. P. (2016). Síntese e caracterização de Fotocatalisadores nanoestruturados de TTNT e Ag3PO4 no espectro visível. PhD Thesis, UFRJ- Escola Politécnica.

Ansari, M. O., R. Kumar, S. Pervez Ansari, M. S. Abdel-wahab Hassan, A. Alshahrie and M. A. E.-F. Barakat (2019). 1 - Nanocarbon aerogel composites. Nanocarbon and its Composites. A. Khan, M. Jawaid, Inamuddin and A. M. Asiri, Woodhead Publishing**:** 1-26.

AspenTech (2012). Ammonia Synthesis with Aspen HYSYS® V8.0- Closed Loop Simulation of Ammonia Synthesis.

Barbosa, I. S. O., J. M. Costa, Y. A. Manrique, M. M. Dias, J. L. Faria, R. J. Santos, C. G. Silva and M. S. C. A. Brito (2023). "ChannelCOMB Device for Mesostructured Reactors and Networks of Reactors." Chemical Engineering & Technology **46**, No.6: 1241-1250.

Barbosa, I. S. O., R. J. Santos, C. G. Silva and M. S. C. A. Brito (2021). "Consecutive Flow Distributor Device for Mesostructured Reactors and Networks of Reactors." Chemical Engineering and Processing - Process Intensification **167**: 108541.

Bojang, A. A. and H.-S. Wu (2020). "Design, Fundamental Principles of Fabrication and Applications of Microreactors." Processes **8**(8): 891.

Boyjoo, Y., H. Sun, J. Liu, V. K. Pareek and S. Wang (2017). "A review on photocatalysis for air treatment: From catalyst development to reactor design." Chemical Engineering Journal **310**: 537-559.

Chen, S., S. Perathoner, C. Ampelli and G. Centi (2019). Chapter 2 - Electrochemical Dinitrogen Activation: To Find a Sustainable Way to Produce Ammonia. Studies in Surface Science and Catalysis. S. Albonetti, S. Perathoner and E. A. Quadrelli, Elsevier. **178:** 31-46.

Chen, X., N. Li, Z. Kong, W.-J. Ong and X. Zhao (2018). "Photocatalytic fixation of nitrogen to ammonia: state-of-the-art advancements and future prospects." Materials Horizons **5**(1): 9-27.

Costa, M. F., C. M. Fonte, M. M. Dias and J. C. B. Lopes (2017). "Heat transfer performance of NETmix—A novel micro-meso structured mixer and reactor." AIChE Journal **63**(6): 2496-2508.

da Costa Filho, B. M., A. L. P. Araujo, G. V. Silva, R. A. R. Boaventura, M. M. Dias, J. C. B. Lopes and V. J. P. Vilar (2017). "Intensification of heterogeneous TiO_2 photocatalysis using an innovative micro-meso-structured-photoreactor for n-decane oxidation at gas phase." Chemical Engineering Journal **310**: 331-341.

Deng, B., Y. Jiang, L. Gao and B. Zhao (2023). "CFD modeling of ethylene degradation in gas-phase photocatalytic reactors." Environmental Science and Pollution Research **30**(9): 24132-24142.

Dharma, H. N. C., J. Jaafar, N. Widiastuti, H. Matsuyama, S. Rajabsadeh, M. H. D. Othman, M. A. Rahman, N. N. M. Jafri, N. S. Suhaimin, A. M. Nasir and N. H. Alias (2022). "A Review of Titanium Dioxide (TiO_2)-Based Photocatalyst for Oilfield-Produced Water Treatment." Membranes **12**(3): 345.

Donnelly, K. and M. Baumann (2021). "Scalability of photochemical reactions in continuous flow mode." Journal of Flow Chemistry **11**.

Duran, J. E., M. Mohseni and F. Taghipour (2011). "Computational fluid dynamics modeling of immobilized photocatalytic reactors for water treatment." AIChE Journal **57**(7): 1860-1872.

Elyasi, S. and F. Taghipour (2010). "Simulation of UV Photoreactor for Degradation of Chemical Contaminants: Model Development and Evaluation." Environmental Science & Technology **44**(6): 2056-2063.

Formenti, M., F. Juillet, P. Meriaudeau and S. Teichner (1971). "Heterogeneous photocatalysis for partial oxidation of paraffins." Chemical technology(NNOV): 680.

Garagounis, I., A. Vourros, D. Stoukides, D. Dasopoulos and M. Stoukides (2019). "Electrochemical Synthesis of Ammonia: Recent Efforts and Future Outlook." Membranes **9**(9): 112.

Han, Z., P. Wu, M. He, X. Zhuang, H. Lin and S. Han (2022). "Ammonia synthesis by electrochemical nitrogen reduction reaction - A novel energy storage way." Journal of Energy Storage **55**: 105684.

Hao, D., J. Ren, Y. Wang, H. Arandiyan, M. Garbrecht, X. Bai, H. K. Shon, W. Wei and B.-J. Ni (2021). "A Green Synthesis of Ru Modified g-C_3N_4> Nanosheets for Enhanced Photocatalytic Ammonia Synthesis." Energy Material Advances **2021**.

Hernández-Alonso, M. D., F. Fresno, S. Suárez and J. M. Coronado (2009). "Development of alternative photocatalysts to TiO_2: Challenges and opportunities." Energy & Environmental Science **2**(12): 1231-1257.

IRENA and AEA (2022). Innovation Outlook: Renewable Ammonia, International Renewable Energy Agency, Abu Dhabi, Ammonia Energy Association, Brooklyn.

Kakaç, S., L. Vasiliev, Y. Bayazitoglu and Y. Yener (2005). Microscale Heat Transfer Fundamentals and Applications: Proceedings of the NATO Advanced Study Institute on Microscale Heat Transfer — Fundamentals and Applications in Biological and Microelectromechanical Systems Cesme-Izmir, Turkey 18–30 July 2004.

Kayahan, E., M. Jacobs, L. Braeken, L. C. Thomassen, S. Kuhn, T. van Gerven and M. E. Leblebici (2020). "Dawn of a new era in industrial photochemistry: the scale-up of micro- and mesostructured photoreactors." Beilstein J Org Chem **16**: 2484-2504.

Li, H., S. Gu, Z. Sun, F. Guo, Y. Xie, B. Tao, X. He, W. Zhang and H. Chang (2020). "The in-built bionic "MoFe cofactor" in Fe-doped two-dimensional MoTe2 nanosheets for boosting the photocatalytic nitrogen reduction performance." Journal of Materials Chemistry A **8**(26): 13038-13048.

Lima, M. J., A. M. T. Silva, C. G. Silva and J. L. Faria (2017). "Graphitic carbon nitride modified by thermal, chemical and mechanical processes as metal-free photocatalyst for the selective synthesis of benzaldehyde from benzyl alcohol." Journal of Catalysis **353**: 44-53.

Lima, M. J., A. M. T. Silva, C. G. Silva, J. L. Faria, J. C. B. Lopes and M. M. Dias (2016). "An innovative static mixer photoreactor: Proof of concept." Chemical Engineering Journal **287**: 419-424.

Lira, J. O. d. B., H. G. Riella, N. Padoin and C. Soares (2022). "Fluid dynamics and mass transfer in curved reactors: A CFD study on Dean flow effects." Journal of Environmental Chemical Engineering **10**(5): 108304.

Marnellos, G. and M. Stoukides (1998). "Ammonia Synthesis at Atmospheric Pressure." Science **282**(5386): 98-100.

Modak, J. M. (2002). "Haber process for ammonia synthesis." Resonance **7**(9): 69-77.

Nguyen, V.-H., M. Mousavi, J. B. Ghasemi, Q. V. Le, S. A. Delbari, M. Shahedi Asl, M. Shokouhimehr, M. Mohammadi, Y. Azizian-Kalandaragh and A. Sabahi Namini (2021). "In situ preparation of g-C_3N_4 nanosheet/FeOCl: Achievement and promoted photocatalytic nitrogen fixation activity." Journal of Colloid and Interface Science **587**: 538-549.

Perera, Y. (2017). Evaporator Unit Design for the Magnesium Sulfate Production plant.

Pirie, M. (2019). "Fritz Haber Fixed Nitrogen." Retrieved 3, May, 2023, from https://www.adamsmith.org/blog/fritz-haber-fixed-nitrogen.

Rouwenhorst, K. H. R., H.-H. Kim and L. Lefferts (2019). "Vibrationally Excited Activation of N2 in Plasma-Enhanced Catalytic Ammonia Synthesis: A Kinetic Analysis." ACS Sustainable Chemistry & Engineering **7**(20): 17515-17522.

Sato, S. and J. M. White (1980). "Photodecomposition of water over Pt/TiO_2 catalysts." Chemical Physics Letters **72**(1): 83-86.

Schrauzer, G. N. and T. D. Guth (1977). "Photolysis of Water and Photoreduction of Nitrogen on Titanium Dioxide." Journal of the American Chemical Society **99**(22): 7189-7193.

Sengupta, T. K., M. F. Kabir and A. K. Ray (2001). "A Taylor Vortex Photocatalytic Reactor for Water Purification." Industrial & Engineering Chemistry Research **40**(23): 5268-5281.

Shen, H., T. Peppel, J. Strunk and Z. Sun (2020). "Photocatalytic Reduction of CO_2 by Metal-Free-Based Materials: Recent Advances and Future Perspective." Solar RRL **4**(8): 1900546.

Shen, H., M. Yang, L. Hao, J. Wang, J. Strunk and Z. Sun (2022). "Photocatalytic nitrogen reduction to ammonia: Insights into the role of defect engineering in photocatalysts." Nano Research **15**(4): 2773-2809.

Silva, É. F. M., E. D. C. Oliveira, A. T. S. Ribeiro, R. R. P. Garcia, D. C. Napoleão, O. Sanz and L. C. Almeida (2022). "A brass-mesh structured photoreactor applied in the photocatalytic degradation of RB5 dye." Chemical Engineering and Processing - Process Intensification **174**: 108895.

Singhal, N. and U. Kumar (2017). "Noble metal modified TiO_2: selective photoreduction of CO_2 to hydrocarbons." Molecular Catalysis **439**: 91-99.

Smith, C., A. K. Hill and L. Torrente-Murciano (2020). "Current and future role of Haber–Bosch ammonia in a carbon-free energy landscape." Energy & Environmental Science **13**(2): 331-344.

Society, T. R. (2020). Ammonia: zero-carbon fertiliser, fuel and energy store.

Sosnowski, M. (2018). "The influence of computational domain discretization on CFD results concerning aerodynamics of a vehicle." Journal of Applied Mathematics and Computational Mechanics **17**: 79-88.

Spiga, M. and G. L. Morino (1994). "A symmetric solution for velocity profile in laminar flow through rectangular ducts." International Communications in Heat and Mass Transfer **21**(4): 469-475.

Starosud, A., A. Bhargava, C. H. Langford and A. Kantzas (1999). Development of New Photo-Catalytic Methods and Reactors for Waste Water Treatment. Studies in Surface Science and Catalysis. G. F. Froment and K. C. Waugh, Elsevier. **122:** 219-228.

UN (2022). 2022 Revision of World Population Prospects, Department of Economic and Social Affairs, Population Division.

Vaiano, V., D. Sannino and O. Sacco (2020). Chapter 10 - Heterogeneous photocatalysis: how doping with nitrogen can improve the performance of semiconductor nanoparticles under visible light irradiation. Nanomaterials for the Detection and Removal of Wastewater Pollutants. B. Bonelli, F. S. Freyria, I. Rossetti and R. Sethi, Elsevier**:** 285-301.

Valera-Medina, A., H. Xiao, M. Owen-Jones, W. I. F. David and P. J. Bowen (2018). "Ammonia for power." Progress in Energy and Combustion Science **69**: 63-102.

Wilke, C. R. and P. Chang's (1955). "Correlation of diffusion coefficients in dilute solutions." AIChE Journal **1**(2): 264-270.

Yüzbaşıoğlu, A. E., C. Avşar and A. O. Gezerman (2022). "The current situation in the use of ammonia as a sustainable energy source and its industrial potential." Current Research in Green and Sustainable Chemistry **5**: 100307.

Zhang, H., Z. Liu, Y. Li, C. Zhang, Y. Wang, W. Zhang, L. Wang, L. Niu, P. Wang and C. Wang (2020). "Intimately coupled TiO_2/g-C_3N_4 photocatalysts and in-situ cultivated biofilms enhanced nitrate reduction in water." Applied Surface Science **503**: 144092.

Appendix A - Velocity Profiles

A.1. User-Defined Function

The function interpreted in all ANSYS/Fluent simulations was based on the work of Barbosa et al. (2021), which reported a dimensionless velocity profile in a rectangular duct, defined from the analytical solution of steady laminar flow in said geometry.

This user-defined function (UDF) was created using the C programming language and it was added to the software as a boundary condition of the inlet face of the unit-cell.

Several assumptions were made in the writing of the function: the fluid was considered a Newtonian fluid with constant properties, natural convection was neglected, the pressure along the flow direction was set as constant and the no-flux condition was established for the walls.

Dimensionless coordinates, $\xi = x/a$, and $\eta = y/a$ were defined according to Figure A1.1. As the inlet channel is a square duct, these two parameters take the same value, making the respective aspect ratio, β, equal to 1.

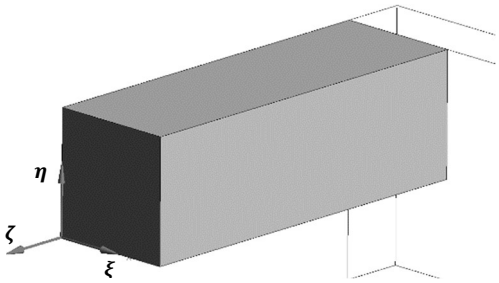

Figure A1.1- Schematic representation of the inlet of the unit-cell.

The dimensionless velocity profile of equation A.1 was defined from the analytical solution of steady laminar flows in rectangular ducts, proposed by Spiga and Morino (1994).

$$v^*(x,y) = \frac{16\beta^2}{\pi^4} \sum_{n\ odd}^{\infty} \sum_{m\ odd}^{\infty} \frac{\sin(n\pi\xi)\sin(m\pi\eta/\beta)}{nm\,(\beta^2 n^2 + m^2)} \tag{A.1}$$

Further simplifications allow using the equation A.2 below

$$v^*(x,y) = v_{in} \times \frac{\sum_{n\ odd}^{\infty} \sum_{m\ odd}^{\infty} \frac{\sin(n\pi\xi)\sin(m\pi\eta/\beta)}{nm\,(\beta^2 n^2 + m^2)}}{\sum_{n\ odd}^{\infty} \sum_{m\ odd}^{\infty} \frac{4}{\pi^2 n^2 m^2 (\beta^2 n^2 + m^2)}} \tag{A.2}$$

as the boundary condition in the inlet. The sinusoidal functions guarantee the symmetry of the distribution with respect to the centre of the channel.

The injection velocity, v_{in}, is the variable parameter, dependent on the Reynolds number of each simulation.

A.2. Inlet Velocity Profiles

The UDF was applied to all case files to impose a 3D parabolic velocity profile for the fluid flow through the rectangular pipe. According to the theoretical profile defined by the function, the expected velocity curve for the inlet channel takes the form of the following graphics of Figures A2.1a) and A2.1b).

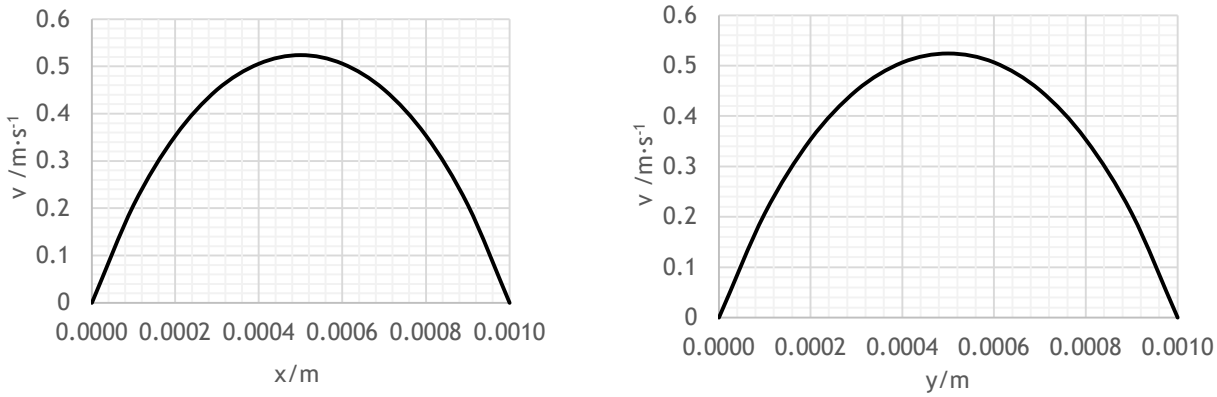

Figure A2.1- Expected velocity profile for a square duct using the UDF for the x-direction (a) and y-direction (b).

Flow inside all generated meshes was tested previous to mass transfer simulations, to ensure a fully developed parabolic profile at the inlet channel, with no changes along the axial direction.

Figures A2.2 and A2.3 compare the parabolic profiles at the inlet face, the middle, and the end ($z = 0$) of the inlet channel, for lengths of 6mm and 3mm, respectively.

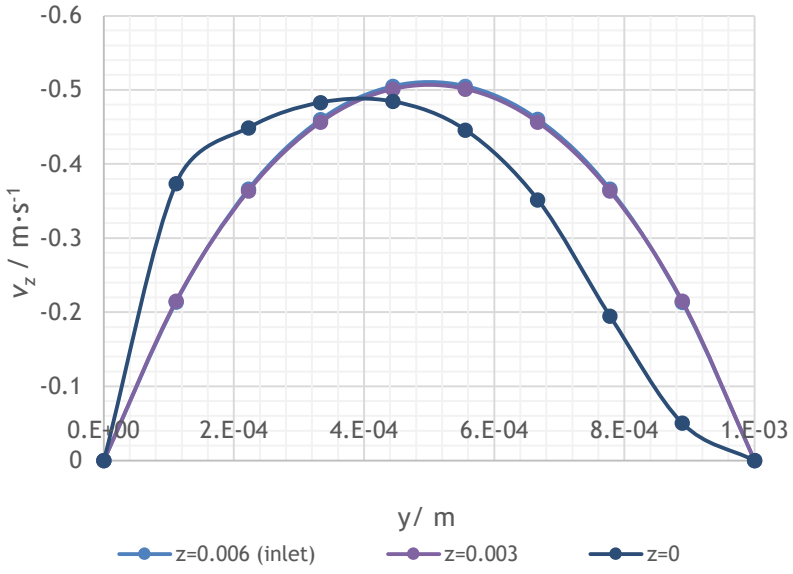

Figure A2.2- Velocity profiles along y-direction for l_{in} =6 mm.

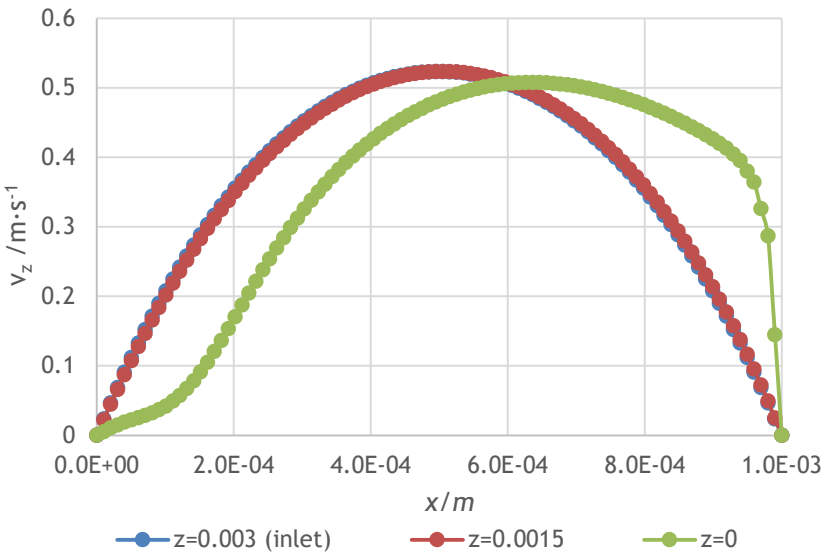

Figure A2.3- Velocity profiles along x-direction for l_{in} =3mm.

As shown, for both cases, the profile remains fully developed throughout the pipe until it reaches the end of the channel. Shortening the length of the distributor in half does not appear to affect the expected parabolic profile, and it substantially minimises the computational time required for further simulations.

It is also to note that, as expected from the model (Figure A2.4), for a $\beta = 1$, the maximum registered velocity was 0.524 m·s^{-1}, about 2.1 times higher than the injection velocity.

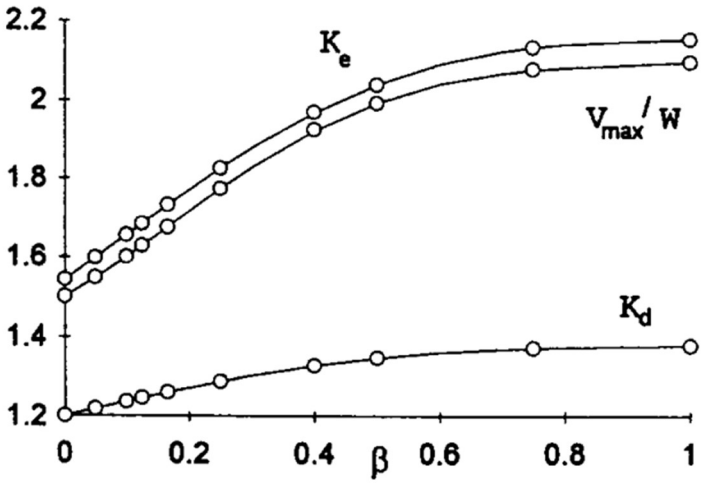

Figure A2.4- Estimative of the expected maximum-to-average velocity ratio. (Spiga and Morino 1994)

Appendix B - Hydrodynamics

The traced path lines for the two different Reynolds tests are presented.

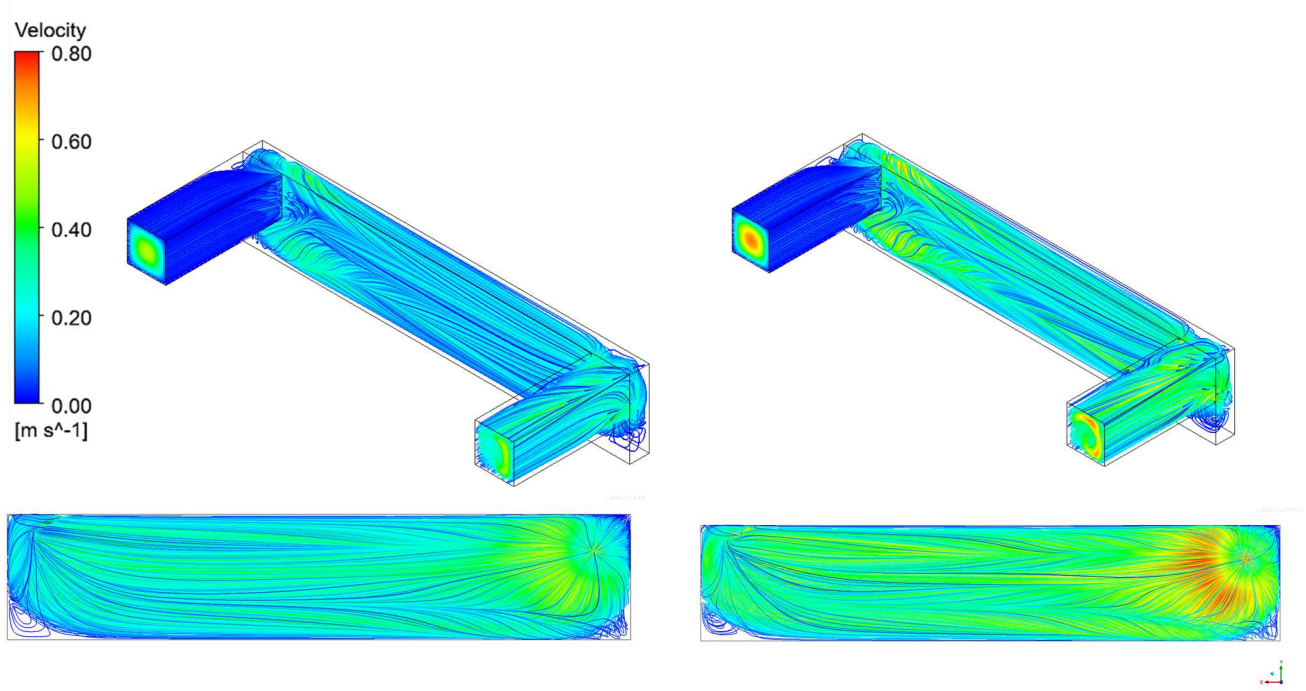

(a) *(b)*

Figure B.1- Velocity path lines of the flow inside the cell for Re= 250 (a) and 350 (b).

Appendix C - Tracer Simulations

Figure C.1 shows a volume rendering approach to visualise simulation data. The mass fraction of tracer inside the DeanCell was monitored along the experiment time, and the contours are represented for a range of $\theta = 0.02$ to $\theta = 5$.

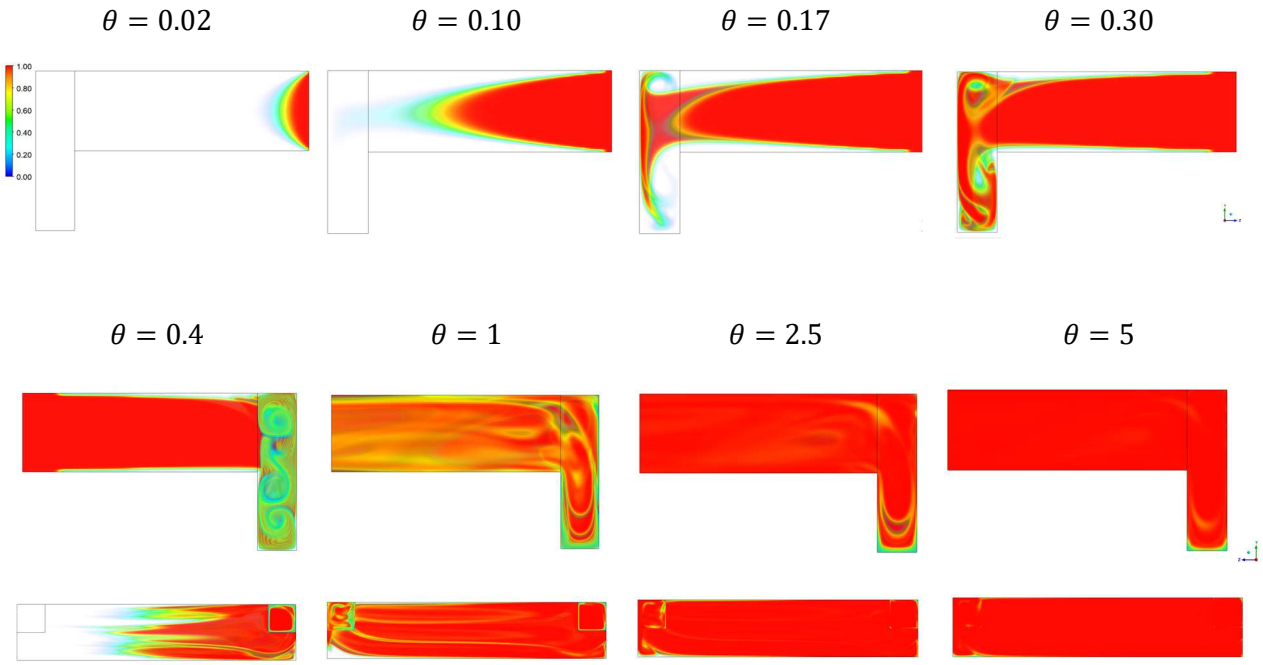

Figure C.1- Contours of tracer mass fraction for the transient RTD experiment.

The contours show a stagnant zone at the end of the main body, near the outlet channel, which can explain the behaviour of the residence time distribution curve. At $\theta = 1$, i.e., the residence time, the outlet mass fraction of tracer is lower than 1, meaning that not all fluid elements have exited the reactor. Even at $\theta = 5$, it is still possible to observe zones of lower fluid velocity at the bottom of the reactor, where the mixing of the fluid phase is not as efficient.

Appendix D - ASPEN Simulations

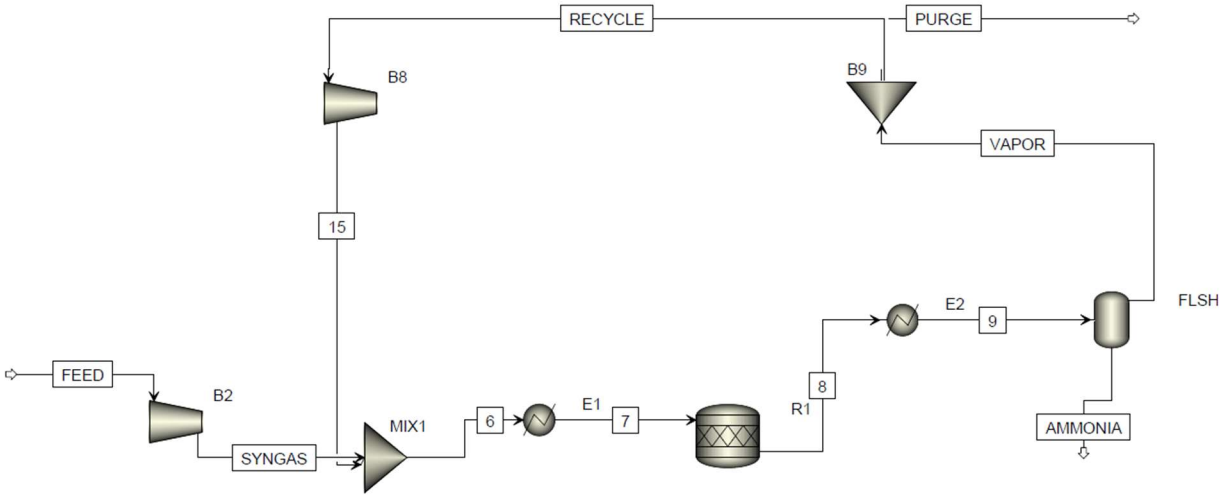

Figure D.1- Simulated Haber-Bosch process flowsheet. Adapted from AspenTech (2012)